LIVERPOOL JOHN MOORES UNIVERSITY

Faculty Research Day

Conference Papers Wednesday 19th May 2021

Sam Stafford

Postgraduate Researcher

Astrophysics Research Institute

Exploring extensions to the standard cosmological model and the impact of baryons on small scales

Sam G. Stafford, Shaun T. Brown, Ian G. McCarthy, Andreea S. Font, Andrew Robertson and Robert Poole-McKenzie

Astrophysics Research Institute, 146 Brownlow Hill, Liverpool, L3 5RF

s.stafford@2014.ljmu.ac.uk

Abstract. It has been claimed that the standard model of cosmology (ΛCDM) cannot easily account for a number of observations on relatively small scales, motivating extensions to the standard model. Here we introduce a new suite of **cosmological** simulations that systematically explores three plausible extensions: warm dark matter, self-interacting dark matter, and a running of the scalar spectral index of density fluctuations. Current observational constraints are used to specify the additional parameters that come with these extensions. We examine the halo mass function in these various cosmologies and find significant degeneracies can be present between the extensions. In detail, however, the different extensions have quantitatively distinct mass dependencies. We compare the derived cosmological trends with the impact of baryonic physics using the *EAGLE* simulations. Significant degeneracies are also present between baryonic physics and cosmological variations (with both having similar magnitude effects on some observables). Given the inherent uncertainties both in the modelling of galaxy formation physics and extensions to ΛCDM, a systematic and simultaneous exploration of both is strongly warranted.

1.   Introduction

The current cosmological paradigm describes a universe which has a matter content that is primarily composed of collisonless cold dark matter (CDM), a cosmological constant (Λ), and normal baryonic matter [1]. The true nature of dark matter, however, is still an unsolved problem. Aside from there not yet being a confirmed direct detection of dark matter, there are also claimed problems with the current cosmological model (the ΛCDM model) on small scales which could hint at a deviation from CDM. For example, three of the most widely discussed issues with this model are the 'cusp–core problem' [2, 3], the 'missing satellites problem' [4, 5], and the 'too-big-to-fail problem' [6].

These issues have fuelled research into alternatives/extensions to the standard model, particularly modifications to the nature of dark matter. For example, one can relax the assumption that dark matter is purely collisonless, allowing instead for a non-negligible self-interaction (as proposed in [7]). Another popular extension retains the assumption that dark matter is collisonless but invokes a non-negligible thermal velocity at early times. Termed warm dark matter (WDM), the associated free-streaming erases small-scale density perturbations leading to a characteristic cut-off in the linear matter power spectrum [8]. This leads to WDM potentially being able to resolve the previous tensions through the lack of formation of small-scale structure (e.g. [9]). An alternative mechanism that can alter small-scale structure, but which treats dark matter in the standard way (cold and collisonless), is to invoke a change in the primordial power spectrum on small scales, by allowing for a running scalar spectral index [10]. [11] have previously shown that a negative running can help resolve the missing satellite problem as well as alleviate the too-big-to-fail problem.

It is possible, however, that the small-scale crises outlined previously which supposedly exist with the ΛCDM model are instead just a product of conclusions drawn from comparing the observable Universe to the predictions from a series of dark matter-only simulations. Recently there has been extensive research into the possibility that a realistic treatment of baryonic physics in simulations, such as supernovae feedback, stellar winds, and feedback from active galactic nuclei (AGN), may be able to resolve some of these tensions. These studies have shown the importance of including baryonic physics in the simulations (see e.g., [12, 13, 14]) and do not require any extensions to the standard model to resolve the apparent small-scale tensions.

2.   Simulations

For this study, we have run a suite of high resolution, cosmological volumes, sampling different possible extensions to the ΛCDM model. The suite consists of 7 dark matter-only, periodic box simulations which are 25 comoving Mpc h^{-1} on a side, each containing 1024^3 dark matter particles. The cosmological parameters for the simulations in this suite use the fiducial Planck 2015 maximum likelihood values [1], apart from the simulations which include a running scalar spectral index (see [15] for details on this). To compare to the impact of baryonic physics, we make use of the high-resolution *EAGLE*-Recal model [16, 17]. The *EAGLE*-Recal simulation has comparable resolution and statistics to our simulations.

3.   Cosmological extensions

The epoch of inflation seeded small density perturbations in the matter distribution of the Universe, with the power spectrum of these perturbations in the ΛCDM model being of the form:

$$P(k) = Ak^{n_s} \quad (1)$$

where $P(k)$ is the power spectrum as a function of wavenumber k, A defines the amplitude of the primordial matter power spectrum, and n_s is the scalar spectral index [18]. In the ΛCDM model, n_s is assumed to be constant, with no k dependence. However, even the simplest models of inflation predict some level of deviation from a power-law distribution. Allowing for running, the modified power spectrum, $P(k)$, can be expressed as [10]:

$$P_s(k) \ = \ A_s(k_0)\left(\frac{k}{k_0}\right)^{n_s(k=k_0)+\alpha_s'(k)} \quad (2)$$

where $\alpha_s'(k) \equiv \left(\frac{\alpha_s}{2}\right)\ln\left(\frac{k}{k_0}\right)$, α_s is the running of the scalar spectral index, which is defined as $dn_s(k)/d\ln(k)$. The pivot scale, k_0, is the scale at which the amplitude of the power spectrum (A_s) is defined, along with the scale at which the spectral index is measured when $\alpha_s \neq 0$. In this study, we adopt the same pivot scale as that used for the cosmological parameter estimation of [1]: $k_0 = 0.05$ Mpc^{-1}.

Instead of modifying the primordial power spectrum, as in the case of a running of the scalar spectral index, the nature of dark matter itself can be modified. Warm dark matter (WDM) differs from CDM in the standard model, in that the subatomic particles that constitute WDM are considerably lighter ($\approx$keV) than CDM particles ($\approx$GeV to TeV masses). Consequently, WDM particles remain relativistic for longer in the early Universe compared with CDM, resulting in non-negligible thermal velocities that allow the particles to free-stream out of small-scale density perturbations, smoothing them out and suppressing the growth of structure on small scales (e.g., [19]).

This smoothing out of density perturbations due to the thermal velocity associated with WDM leads to a characteristic cut-off in the WDM power spectrum. This effect can be modelled as a transfer function $T_{\mathrm{WDM}}(k)$ relative to the CDM power spectrum:

$$P_{\mathrm{WDM}}(k) = T_{\mathrm{WDM}}^2(k)P_{\mathrm{CDM}}(k) \quad (3).$$

Another possible extension to the ΛCDM model is to allow the dark matter particles to self-interact (i.e., scatter with neighbouring particles). Here the dark matter is still assumed to be cold initially as in the standard model. The dark matter interactions are assumed to be fully described by an azimuthally-symmetric differential cross-section, defined in the centre of momentum frame of the two particles. We only examine the case where the scattering events are velocity independent and isotropic. Under these assumptions, the interactions are described by a differential cross-section (which is the rate at which particles are scattered into a region of solid angle) equal to:

$$\frac{d\sigma}{d\Omega} = \frac{\sigma}{4\pi} \quad (4).$$

4.   Spherical Overdensity Mass Function

In this section we discuss the differences which arise in the Spherical Overdensity (SO) mass function, shown in Figure 1, in these different cosmological models (and when one has a realistic treatment of baryonic physics). Here we define the SO halo mass function as the number density of haloes which exist per logarithmic mass interval: $\phi \equiv \frac{dn}{d\log_{10}(M)}$, which in this study is plotted as a function of SO mass: $M = M_{200,\mathrm{crit}}$. This is defined as the mass contained within a radius $R_{200,\mathrm{crit}}$, which encompasses an overdensity $200 \times$ the critical density of the universe. Haloes in this study are identified using the SUBFIND algorithm [20, 21] which uses a Friends-of-Friends (FoF) algorithm [22] to link all particles which have a separation less than some fraction of the mean inter-particle separation (with this fraction being set to 0.2 in this study).

Focusing first on the cosmologies which have a running scalar spectral index as a free parameter, it can be seen in Figure 1 that there is a relatively large suppression ($\approx$10-20%) in the number density of haloes with $M_{200,\mathrm{crit}} \lesssim 10^{11} M_{\odot}\, h^{-1}$ for the case with a negative running cosmology. This is best illustrated in the bottom panel of this plot, which shows the HMF of each cosmology normalised with respect to the reference simulation.

Conversely the opposite is seen for the cosmology which has a positively-running scalar spectral index, which sees an $\approx$ 10% increase in the number density of haloes at these masses. These results illustrate how relatively

subtle changes to the primordial matter power spectrum can have relatively large effects on the growth of structure on small scales.
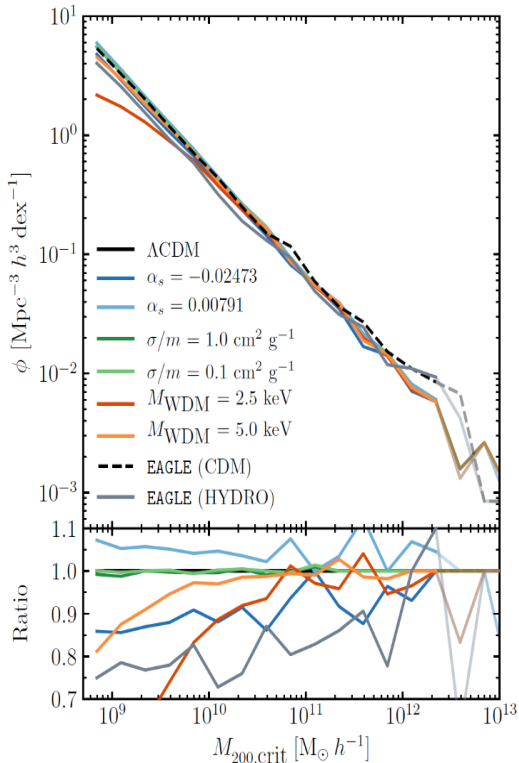

Figure 1: Top: number density of haloes per logarithmic mass interval, plotted as a function of their spherical overdensity mass. Bottom: the results in the top panel normalised with respect to the ΛCDM result. Note for the EAGLE simulations, the hydrodynamical simulation result is normalised with respect to the result from the complementary dark matter-only simulation. The lines become transparent for mass bins which have fewer than 10 haloes.

Like the effects of a negative running cosmology, switching to WDM also leads to a significant suppression in the mass function at low masses. As expected, the effect is largest in the simulation with the lighter WDM particle mass. This is a well-known result, having been found for a range of WDM masses and models previously (e.g., [23]).

Examining the simulations where the dark matter can self-interact, there is no significant effect on the number density of SO haloes which form. This agrees with previous results that have been found when comparing large-scale statistics in SIDM and CDM cosmologies [24].

We now compare the previous effects, present due entirely to changes in the cosmological model, to those present in fully hydrodynamic simulations in the context of the standard model. Examining the result from the EAGLE simulation, it is interesting that the suppression seen in the HMF is bracketed by the results for the two WDM cosmologies, and the cosmology with a negative running. For example, the EAGLE simulation predicts a suppression of around 20% for haloes with mass around 10^9 M$_\odot$ h^{-1}, whereas the suppression seen in the different cosmologies range between $\approx$ (15-50) %. Physically, the suppression of the halo mass function in the hydrodynamical simulations is the result of ejection of baryons due primarily to stellar feedback at these mass scales.

Another interesting feature is how the suppression of the halo mass function as a function of mass in the EAGLE run is closely mimicked by the result seen for a (dark matter-only) cosmology with a negative running, at least in shape. Furthermore, as was shown in [15], baryonic effects and the effects from the inclusion of a running spectral index appear to be separable to within a few percent, with each effect treatable as a multiplicative correction to the HMF of a ΛCDM gravity-only simulation. As such, in the presence of an (unaccounted for) positively-running scalar spectral index, one would tend to underestimate the role of baryons in suppressing the HMF. This problem is compounded by the current uncertainty in the suppression of the HMF due to baryonic physics on these scales. This is because current observations measuring the gaseous component of haloes on these scales [25, 26, 27] - which are a proxy for how efficient stellar feedback is at removing baryons from these haloes - are themselves quite uncertain. This propagates through to poor constraints on the stellar feedback implemented into hydrodynamical simulations.

5.   Discussion and Conclusions

In this study we have systematically explored different proposed mechanisms for altering the distribution of matter on small scales. This includes alterations to the standard model of cosmology or including baryonic effects within the standard model. These mechanisms are motivated in part by apparent tensions between the standard model and observational data in the local Universe. The main findings of our study may be summarised as follows:

- Baryonic physics, WDM, and a running spectral index alter the spherical-overdensity (SO) halo mass function (Figure 1) in similar ways and are expected to be degenerate if they are constrained solely using this metric. A cosmology where the DM can self-interact (SIDM) is the only cosmological extension examined here which has no significant effect on the SO halo mass function.

The different cosmological extensions explored here can produce large, and potentially measurable effects on the structure which forms in the Universe. All the cosmological extensions examined are within current observational constraints and can potentially alleviate some of the small-scale crises which (may) exist with the standard model of cosmology. An interesting problem arises, however, in that some of the models have

highly degenerate effects. As such, when making constraints on these different cosmological extensions, it is potentially necessary to combine probes which examine different aspects of haloes and their satellite subhaloes in order to break degeneracies between the different extensions. This is because, in detail, the different extensions do have different mass dependencies which can be exploited to simultaneously constrain them.

However, it is important to note that this study has focused on dark matter-only simulations when extending ΛCDM. We examined the *EAGLE*-Recal simulation to compare the results from these gravity-only simulations to those from full hydrodynamical simulations (in the context of the standard model). We find that baryonic physics can also be highly degenerate with varying the cosmological model. While it is clear that baryonic effects are important, how robust the predictions are remains an open question. Since feedback efficiencies cannot be predicted from first principles and must therefore be calibrated against some set of observable properties of galaxies [16], there is a danger that we may come to erroneous conclusions about the role of baryons if those calibration observables also depend on cosmology.

6.   References

[1]   Planck Collaboration, *A&A,* p. 594, 2016.

[2]   R. A. Flores and J. R. Primack, *ApJ,* vol. 427, p. L1, 1994.

[3]   B. Moore, *Nature,* vol. 370, p. 629, 1994.

[4]   A. Klypin, A. V. Kravstov, O. Valenzuela and F. Prada, *ApJ,* vol. 522, p. 82, 1999.

[5]   B. Moore, S. Ghigna, F. Governato, G. Lake, T. Quinn, J. Stadel and P. Tozzi, *ApJ,* vol. 524, p. L19, 1999.

[6]   M. Boylan-Kolchin, J. S. Bullock and M. Kaplinghat, *MNRAS,* vol. 415, p. 40, 2011.

[7]   D. N. Spergel and P. J. Steinhardt, *PRL,* vol. 84, p. 3760, 2000.

[8]   J. R. Bond, G. Efstathiou and J. Silk, *PRL,* vol. 45, p. 1980, 1980.

[9]   P. Colin, V. Avila-Reese and O. Valenzuela, *ApJ,* vol. 542, p. 622, 2000.

[10]   A. Kosowsky and M. S. Turner, *PRD,* vol. 52, p. R1739, 1995.

[11]   S. Garrison-Kimmel, *et al.*, *MNRAS,* vol. 471, p. 1709, 2017.

[12]   S. Mashchenko, J. Wadsley and H. M. Couchman, ," *Science,* vol. 319, p. 174, 2008.

[13]   A. Fitts, *et al.*, *MNRAS,* vol. 471, p. 3547, 2017.

[14]   J. S. Bullock, A. V. Kravtsov and D. H. Weinberg, *ApJ,* vol. 539, p. 517, 2000.

[15]   S. G. Stafford, *et al.*, *MNRAS,* vol. 493, p. 676, 2020.

[16]   J. Schaye, *et al.*, *MNRAS,* vol. 446, p. 521, 2015.

[17]   R. A. Crain, *et al.*, *MNRAS,* vol. 450, p. 1937, 2015.

[18]   A. H. Guth, *PRD,* vol. 23, p. 347, 1981.

[19]   J. R. Bond and A. S. Szalay, *ApJ,* vol. 274, p. 443, 1983.

[20]   V. Springel, S. D. M. White, G. Tormen and G. Kauffmann, *MNRAS,* vol. 328, p. 726, 2000.

[21]   K. Dolag, S. Borgani, G. Murante and V. Springel, *MNRAS,* vol. 399, p. 497, 2009.

[22]   M. Davis, G. Efstathiou, C. S. Frenk and S. D. M. White, *ApJ,* vol. 292, p. 371, 1985.

[23]   R. E. Smith and K. Markovic, *PRD,* vol. 84, p. 1, 2011.

[24]   M. Rocha, *et al.*, *MNRAS,* vol. 430, p. 81, 2013.

[25]   R. Giovanelli, *et al.*, *AJ,* vol. 130, p. 2598, 2005.

[26]   T. Brown, *et al.*, *MNRAS,* vol. 466, p. 1275, 2017.

[27]   M. P. Haynes, *et al.*, *ApJ,* vol. 861, p. 49, 2018.

Veronica Torres de Sande

Postgraduate Researcher

School of Civil Engineering and Built Environment

Future steps in the investigation of concrete containing waste materials: the case of SCB FA exposed to marine environment

V. Torres de Sande[a], **M. Sadique**[a], **A. Bras**[a], **P. Pineda** [b]

[a] Built Environment and Sustainable Technologies (BEST) Research Institute, Department of Built Environment, Liverpool John Moores University, Byrom St., Liverpool, L3 3AF, UK.
[b] Department of Building Structures and Geotechnical Engineering. School of Architecture. Universidad de Sevilla, Avda. Reina Mercedes, 2, 41012, Seville, Spain.
E-mail address: v.torresdesande@2018.ljmu.ac.uk

Abstract. Efforts are made to incorporate new eco-efficient materials in concrete to mitigate the environmental impact of concrete production and usage. Most of research focuses on mechanical and rheology performance; less research addresses the durability properties. In this research, the use of high-containing quartz industrial sugarcane bagasse fly ash as sand replacement in cement-based materials is investigated. Durability-related tests (open porosity test, electrical resistivity test, capillary absorption test and chloride migration test) have been conducted at 28, 60, 90 and 240days. SCB FA showed being an enhancer of durability-related properties of the concrete due to the capability of modifying the microstructure of the concrete obtaining reductions on the chloride migration coefficients up to 47.9%. Based on the physico-chemical characteristics of ashes and the first results of the concrete performance, additional binding capacity of chlorides ions can be expected resulting in an extended service life of the structure. This research also demonstrates the inadequacy of establishing conclusions based on durability tests when run independently, since direct correlations do not always occur when using unexplored materials. Based on the results future steps in the investigation of these materials have been drawn and importance of the use of proper analytical techniques highlighted.

Keywords. Waste materials, concrete durability, circular economy, sustainable materials.

1. Introduction

Nowadays, as a response to the environmental awareness, efforts are put in the production of new eco-efficient materials by incorporating waste as cement or aggregates replacements, by enhancing the durability properties of the concrete or by using self-healing techniques. Biomass ashes are widely investigated as eco-efficient alternate materials to cement or aggregates in concrete. In addition, biomass ashes have lower greenhouse gas emissions ($\downarrow$ 9.46-57.52%) and lower embodied energy ($\downarrow$1%-17.45%) [1]. As widely accepted industrial waste used as supplementary cementitious materials (SCMs), FA, SF, MK or GGBS, some non-normalised waste materials such as biomass ashes have shown to provide enhanced properties to the concrete: gains in the compressive strength, and/or reductions in the diffusion of chlorides -main responsible of one of the most common and severe causes in early deterioration and the service life reduction of infrastructures- [1-4]. The refinement of the pore structure due to a filler effect and the block of the channels because of the pozzolanic activity are accepted as the main responsible mechanisms. Pozzolanicity of industrial biomass ashes is limited due to the combustion processes, thus high energy consumer treatments are needed when cement is meant to be substituted. In addition, widely accepted correlation between physical characteristics of concretes (e.g. high porosity lead to less compressive strength and less chloride penetration resistance (CPR), or high capillary absorption may lead to low CPR), must be put into question when unexplored materials are investigated [4,5]. In this research, the durability properties of concretes containing industrial sugarcane bagasse ash (SCB FA) with high content in quartz as sand substitute, are explored. By means of a range of performance-based tests, the existing correlations in relation to age of curing and substitution rates are investigated. Based on the results, the potentialities and future steps are drawn.

2. Materials and methods

2.1. Materials
Ordinary Portland Cement, OPC, CEM I, 52.5 N, as per BS EN 197-1: 2011, <600 mμ natural dried sand, 10mm and 20mm aggregates as per BS EN 12620:2002+A1:2008 and industrial sugarcane bagasse fly ash (SCB FA) were used. Table 1 shows chemical composition of OPC and SCB FA.

2.2. Methods
As-received ashes were sieved, partially water washed and physically and chemically characterised. Four bio-concrete mixes were casted using SCB FA as sand replacement (substitution rates: 0%, 10%, 20% and 30% by weight) and constantly water cured until testing according to table 2.

Table 1. Chemical composition.   **Table 2.** Concrete testing summary table.

Element, %	OPC	SCB FA
SiO_2	26.66	60.92
Al_2O_3	2.22	7.62
Fe_2O_3	2.43	5.99
CaO	64.11	11.84
MgO	1.55	2.78
K_2O	0.64	2.25
Na_2O	0.27	1.24
TiO_2	1.33	0.58
P_2O_5	0.87	0.25
MnO	0.15	0.17
Cl^- (soluble)	-	0.10

Physical and chemical properties	Tests	Age (days)
Consistency (Slump test)	BS EN 12350-2	0
Density of fresh concrete	BS EN 12350-6	0
Density of hardened concrete	BS EN 12390-7	28
Compressive strength	BS EN 12390-3:2019	28
Water absorption due to capillary	BS EN 1015-18:2002	28, 60, 90, 240
Total open porosity	BS EN 1936: 2006	28, 60, 90, 240
Chloride migration of concrete	NT Build 492	28, 60, 90, 240
Surface electrical resistivity	Wenner four-probe system	28, 60, 90, 240

3. Results and discussion

3.1. Results

The results show a clear positive progression over time on concretes containing SCB FA with repercussion on the durability performance of the concrete. Figure 1 shows the comparison of results of concretes containing 10% and 30% (SCB FA 10 and SCB 30, respectively) to the control concrete. In terms of open porosity, most of the evolution occurs between 28 - 60 days, meanwhile negligible changes take place after 90 days. Although SCB FA 30 mix shows a higher initial open porosity, the velocity rate double that of SCB FA 20 and SCB FA 10, achieving the value of the control concrete after 240 days, attributable to a retarded pozzolanic reaction proportional to the amount of ashes. Similar trend is observed in terms of chloride migration rates, where differences between 10% and 20% of substitution rates are minimal in comparison to 30%. The formers follow the tendency of the control concrete migration curve meanwhile for 30% of replacement a different trend can be observed entailing a faster chloride diffusion resistance development for higher substitution rates. This concords with other authors [6, 7] who concluded that the CPR improvement is more influential than the compressive strength gain when SCB FA is used. In addition, the higher the substitution rate is, the steeper the superficial electrical resistivity curves are, turning away from the control concrete curve. Therefore, it can be noted that SCB FA has potential uses as enhanced-properties alternate sand, where the amount of substitution rates highly influences the final performance of the concrete.
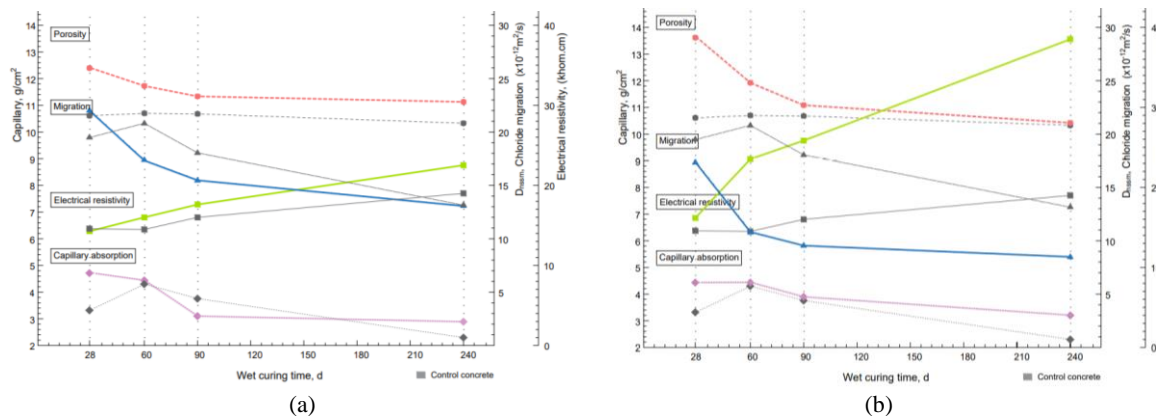

Figure 01. Durability performance over time of SCB FA 10 (a) and SCB FA (b).

3.2. Discussion of the results

The addition of SCB FA decreases the density of concretes, increases the open porosity and the capillary absorption but, in contrast, increases the chlorides penetration resistance. Although the positive evolution over time can be attributable to a densification of the matrix produced by the hydration products resulting from the delayed pozzolanic reaction, changes in the pore distribution and chloride binding phenomenon could be behind the increase in the chloride penetration resistance for concretes with same or higher open porosity. Similar performance was observed by other authors when artificial pozzolans such as FA and MK were used in concrete [8]. Notwithstanding the observation of any chloride binding capacity by means of rapid migration tests have been put into question [9], it is unavoidable to presume its potential existence based on the higher content of C_3A, the generation of secondary hydration products and the high specific surface area.

3.2.1 Potential CBC based on the aluminates content

Aluminates are known to be responsible for chemically bind admixed chlorides forming chloroaluminates (Friedel´s salt mainly, FS), meanwhile external chlorides would only be bound by the remaining available aluminates [10]. The aluminates content in SCB FA would supply more available aluminates able to bind both, internal and external chlorides. This is particularly important to mitigate the effect of admixed chlorides

9

contained in ashes even after been washed, therefore these could be chemically bound in more stable bonds extending the initiation period of corrosion.

3.2.2 Potential role of silicates in CBC
Chlorides can also be physically bound on the surface of hydration products such as CSH gel -mainly- or FS. The pozzolanicity of SCB FA entails the generation of secondary CSH gel through the consumption of $Ca(OH)_2$ thus potentially, more chlorides could be physically bound. Nevertheless, future investigations should also consider the Ca/Si ratio, which is believed to influence the CBC, to optimise the mix formulation or even to increase the amount of substitution rate. Adsorbed chloride ions are more prone to be released than chemical bound chlorides.

3.2.2 Other factors to consider in terms of CBC
Caution should be taken in future investigations on concretes containing SCB FA with high amounts of C_3A under sulfate attack risk. In addition, the effect of the addition of SCB FA in the pH of the concrete should be considered since pH drives changes in the equilibrium of the pore solution promoting the anion exchange. On the other hand, the high specific surface area of ashes and the char particles could physically bind chlorides onto the surface [7,11].

4. Future steps in the research of concrete containing SCB FA
Considering the observations made above, future steps in the investigation of SCB FA based on the use of analytical techniques can be drawn. The aim is to elucidate the generation and influence of the formed hydration products over time and under different environmental exposures. This entails not only the CBC of the matrix, but other RC structures durability-related areas as summarised in table 3.

Table 3. Application areas of analytical techniques.

	Related to	Application of Analytical Techniques
Internal factors	Composition	(a) Quantification and identification of formed hydration products over time. • Soundness of the matrix • Assessment of risks and incompatibilities due to undesirable elements • Identification of mechanisms behind enhanced performances
	Transport mechanism	(b) Ascribing responsibility of pore structure modification to: • Hydration of un-hydrated cement particles • Later pozzolanic hydration → formation of new hydrates • Biological deposition (self-healing)
	Binding of chloride ions	(c) Ascribing responsibility of changes in chloride ions penetration related to: • the amount of hydration products able to adsorb chlorides. • the amount of hydration products able to chemical bind chlorides.
External factors	Exposure (Severity of environment)	(d) Identification of changes in (a, b, c) due to: • Type and concentration of external aggressive species • Temperature and relative humidity • Wetting and drying cycles • External mechanical actions (Erosion, abrasion)

Therefore, the use of sets of appropriate analytical techniques becomes of high importance to assess the kinetics and influence of the resulting hydration products, the stability of the compounds formed, the phase assemblages and the existence of undesirable interactions when concretes are exposed to the marine environment. By using a combination of thermogravimetric tests (TGA-DTA, DTG), Fourier transform-infrared spectroscopy (FT-IR) and X-ray diffraction analysis (XRD) identification, stability, conversion and progression of crystalline hydration products (portlandite, calcium carbonates, mono-carboaluminates, Friedel´s Salt, Kuzel´s salt, etc.) can be obtained [2, 5]. In the case of amorphous CSH, XRD is not suitable, meanwhile silicon nuclear magnetic resonance (^{29}Si NMR) can be used in combination with the other tests. This methodology can be used to identify the vulnerabilities and occurring mechanisms, to compare the influence of each exposure to the control specimen and to assess the variability as a function of depth and time.

Table 4. SWOT analysis on the investigation of SCB FA under marine exposure.

Strengths	Weakness
Gain of deeper understanding in the formation of the hydration products. Obtention of experimental data to have more accurate life prediction models.	Lack of long term - real cases under real exposures. Wide range of variables and scenarios. Lack of homogenization in the criteria.

Opportunities	Threats
Development of more eco-efficient formulations based on optimal performance. Development of solutions to stem the deleterious mechanisms.	Efforts vs. the actual heterogeneity of industrial waste may lead to a lack of interest.

5. Conclusions

The following conclusions have been done:

- The use of SCB FA as sand replacement not only reduces the consumption of natural resources but positively enhances the durability of concretes.
- The chlorides penetration resistance increases with increasing substitution rates of SCB FA.
- High aluminates content may lead to fix admixed chlorides contained in SCB FA and supply additional available aluminates to bind external chlorides.
- The formation of secondary hydration products and the high surface area of ashes enable to expect an increase of the CBC of concretes containing SCB FA, extending the initiation period of corrosion and the service life of structures.

In view of the results, it can be highlighted the importance of further investigation based on analytical techniques when unexplored waste materials are investigated, specifically under the action of external chlorides action. This will facilitate a thorough understanding on the mechanisms behind the interaction of the formed hydration products under different scenarios. Potential areas of application of analytical techniques in combination to other performance-based durability test have been drawn, being this applicable in the investigation of other unexplored SCM.

References:

[1] González-Kunz R N, Pineda P, Bras A, Morillas L 2017, *Sustainable Cities and Society* **31** 151-172.

[2] Kadhim A, Sadique M, Al-Mufti R, Hashim K 2020, *Journal of Building Engineering* **32** 101766.

[3] Minnu S N, Bahurudeen A, Athira G 2020, *Journal of Cleaner Production* 124836.

[4] Torres de Sande V, Sadique M, Pineda P, Bras A, Atherton W, Riley M 2021, *Journal of Building Engineering*.

[5] Chen P, Ma B, Tan H, Liu X, Zhang T, Qi H, Peng Y, Yang Q, Wang J 2020, *Construction and Building Materials* **231** 117171.

[6] Rerkpiboon A, Tangchirapat W, Jaturapitakkul C 2015, **101** 983-989.

[7] Franco-Luján V A, Maldonado-García M A, Mendoza-Rangel J M, Montes-García P 2019, *Construction and Building Materials* **198** 608-618.

[8] Wang Y, Shui Z, Gao X, Yu R, Huang Y, Cheng S 2019, *Construction and Building Materials* **198** 207-217.

[9] Andrade C 2002, *Third RILEM workshop on Testing and Modelling the Chloride Ingress into Concrete, Spain.*

[10] Zibara H 2001, *University of Toronto*.

[11] Yoon S, Moon J, Duan X, Giannelis E, Monteiro P 2014, Chloride adsorption by calcined layered double hydroxides in hardened Portland cement paste, *Materials Chemistry and Physics* **145** 376–386.

Sin Ying Tan

Postgraduate Researcher

School of Computer Science and Mathematics

Students' readiness in facing industrial revolution 4.0 among computing related undergraduates

Sin Ying Tan, Dhiya Al-Jumeily and Abir Hussain
Department of Computer Science, Byrom Street, L3 3AF
E-mail address: s.y.tan@2013.ljmu.ac.uk

Abstract. The intensive technological developments of recent years, such as sensors, autonomous robots or smart networks have paved the way for Industry 4.0 and evolution of education. Recent developments in technology put a strong emphasis on fully equipped graduates that are ready to face the challenges of Industry 4.0. Graduates must be willing to adapt to the rapid changes in the industry and learn new skills as they move along their career. Thus, learning agility is the concept that is used in the proposed integrated framework that is created using design science research methodology. The framework would serve as a tool with steps and processes for students to follow. The framework was evaluated using a survey done with the industry employers. Since there is an increasing demand for fully equipped graduates, a framework exclusively covering the concept of learning agility that also integrates with attitude, technical knowledge and skills falls short. Our framework can support both practice and research by providing a common background that relates the ways, steps, processes, and activities in the different domains to one single common reference.

Keywords. Attitudes, skills, knowledge, learning agility

1. Introduction

The evolution of the industry, which progresses from 1.0 to 4.0, can be used as a sign to show that education should also be developed and evolved from Education 1.0 towards Education 4.0. The industry has undergone a process of digital transformation, which exposes the education to challenges, and opportunities of meeting the needs of the fast-growing industry. The changes in the industry development (industrial revolution) will also cause changes to the development of education (education revolution). Therefore, the need to produce graduates that can solve problems using creative, innovative and critical thinking amid ambiguity has become an imperative for higher education and industry alike.

As the fourth industrial revolution is an era of rapid change where advances in technology are disrupting the way we work and live, the concept of learning agility is integrated in our learning framework to help support students in their learning process to face Industry 4.0. As organisations are continuously changing, growing, shifting, restructuring, downsizing and acquiring new people and resources while frequently investing in new and advanced technologies, a continuous learning & development framework that encourages a lifelong learning culture could be the most decisive factor in producing future learning agile graduates.

2. Background

2.1. Current status of Industry 4.0

There are many industrial research studies done by Siemens, Cisco, PWC, Deloitte, and others. Looking at all of these contributions from academia and industry and the broad range of different interests that they encompass a question arises on the current status of the Industry 4.0. The UK government has also conducted Made Smarter Review as they can see the potential of Industry 4.0. Various research studies have done to help assess the readiness of UK to embrace the concept of Industry 4.0. Research reports show that 67% of the manufacturers recognize the opportunity of Industry 4.0 [1] but only 12% have undertaken strategies to move into the new era. These driving forces have made the fourth industrial revolution to become one of the most frequently discussed topics of many manufacturing conferences, forums and exhibitions in the past few years.

2.2. Pace of education and industrial revolution

Due to the new industry era, technology grows rapidly and there are so many new inventions. However, the author argued that at the beginning of 21st century, the education does not change at a rapid pace as the structures of education are still the same as in the 20th century [2]. The Talent Shortage Survey and the research that was conducted has clearly shown that we are still not ready yet [3,4]. In addition, UK is also facing the critical level in terms of skills shortages risking the country's growth [5]. Moreover, in the most recent World Economic Forum, Jack Ma the founder of Alibaba Group mentioned that the knowledge based approach of 200 years ago would cause our kids to fail as they would never be able to compete with machines and they should be taught soft skills like independent thinking, values and team-work and these mentioned skills can be tackled by first understanding their behaviour and attitudes towards learning [6]. Justin Trudeau also spoke the importance of education in equipping his country for the Industry 4.0.

2.3. Learning Agility

Learning agility is defined as ''the willingness and ability to learn new competencies in order to perform under first-time, tough, or different conditions''[7]. Derue, et al, sought a narrower focus, that they refer learning agility as someone who is quick and flexible in learning from experience in organizations"[8]. Burke also embraces the elements of speed and flexibility, but elaborates it further into describing learning agility "as the engagement in learning behaviours to enhance the capacity to reconfigure activities quickly to meet the changing demands in the task environment"[9]. An agile individual will evaluate the current situation within the context of their past knowledge and experiences and make decisions based on their assessment of the applicability of those experiences to the current situation. Burke has segregated learning agility into nine dimensions which are speed, flexibility, feedback-seeking, interpersonal risk-taking, performance risk-taking, information-gathering, collaborating, experimenting and reflecting [9] while Mitchinson and Morris had put these dimensions into five categories which are innovating, performing, reflecting, risking and defending [10].

3. Methodology

Qualitative approach is used to further explore the current industry's background understanding on Industry 4.0 and to help to identify future trends. As in-depth understanding of the current industry's experiences and problems, future needs that are required might be able to identified. This interview is done with industries so that the important learning behaviours of graduates can be identified [11]. The interview result has actually shown that the attitude of students is actually more important than the knowledge and skills because the future industry is always full with uncertainties, the students could only learn new skills and knowledge if they are willing to learn and meet the changing demands quickly. This explains that it's important to integrate the learning agility concept with the learning framework in supporting students to embrace the challenges of industry 4.0.

Since our research is focused on creating a framework that seeks to increase human and organizational capabilities, the design science research methodology (DSRM) is used [12]. Integrating the framework with the design science research methodology [13], the research is structured into the six phases as shown in table 1: problem identification, objectives definition, design and development, demonstration, evaluation and communication.
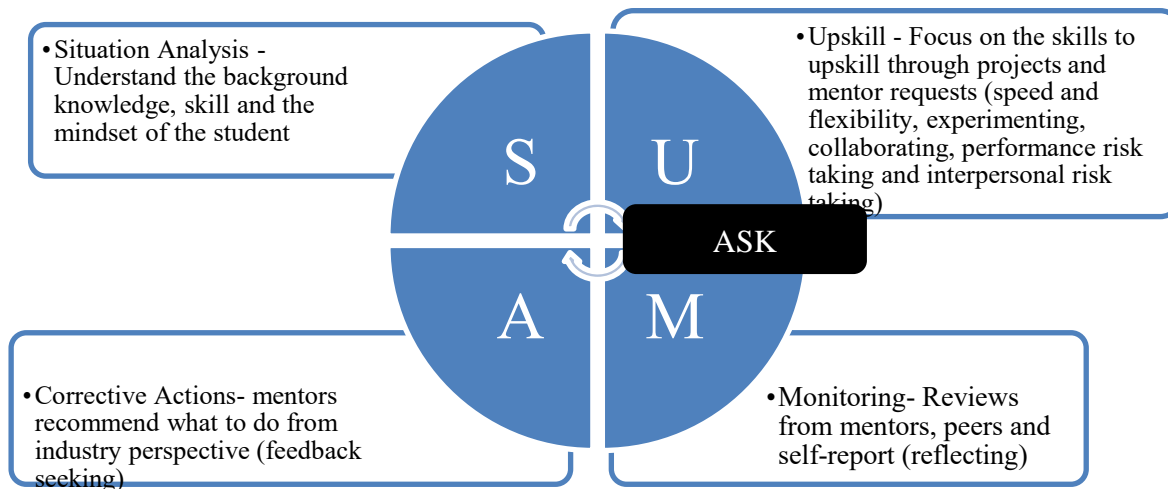
Table 1. DSRM-Identifying the main components of framework

Step	DSRM Activities	Activity Description
1	Problem identification and motivation	Identifying the industrial requirements of the individual to embrace the challenges of industry 4.0.
2	Define the objectives of a solution	To understand the situation and analyse it. To help improve and monitor the students' attitude, skills and knowledge using learning agility concept. To give feedback on the student's progress.
3	Design and development	Design a prototype so that the industry practitioners can evaluate.
4	Demonstration	Demonstrate the use of the artifact and involve the views of experts.
5	Evaluation	Review the results and obtain feedback.
6	Communication	Communicate the findings of the evaluation to relevant audiences.

4. Proposed Framework
*4.1. "ASK SUMA" framework*

Figure 1. *ASK SUMA Framework*

- Situation Analysis - Understand the background knowledge, skill and the mindset of the student
- Upskill - Focus on the skills to upskill through projects and mentor requests (speed and flexibility, experimenting, collaborating, performance risk taking and interpersonal risk taking)
- Corrective Actions- mentors recommend what to do from industry perspective (feedback seeking)
- Monitoring- Reviews from mentors, peers and self-report (reflecting)

"ASK SUMA" integrates with the nine dimensions of learning agility that are speed, flexibility, feedback-seeking, interpersonal risk-taking, performance risk-taking, information-gathering, collaborating, experimenting and reflecting (Burke) and also innovating (Mitchinson and Moris, 2012) and consists of four stages which are Situation Analysis, Upskill, Monitor and Actions as shown in figure 1. First, it is important to understand the student's background knowledge, skills and the mindset in embracing the challenges of future industry. Then, the next stage is Upskill which involves planning strategies to overcome the problems identified in the first stage. Students can get involved in small tasks and projects in this stage to help develop and improve what they are lacked. The next stage in ASK SUMA will be the "Monitor" stage. It is important to monitor the performance of the actions so that one can find out the weakness of the strategy to make improvement. In this stage students can get feedback from mentors and peers or self-report. Finally, the last stage will be corrective action. After reviewing the strategies planned in second stage, corrective actions are taken and the status of the student will be reanalysed as time passes because technology will keep growing and the demands will change according to the requirements of the industry.

4.2. Evaluation of Framework

A short survey was conducted to evaluate the effectiveness of the framework in creating a continuous learning culture that promotes the learning agility concept that is important for students to understand and possess in order to face the challenges of future industry. Table 2 and figure 2 shows the result of the survey.

Types of Responses	%	Count
Yes	90.0	27
No	0.0	0
Not sure	10.0	3

Figure 2. Do you think this framework is effective in helping students to be ready to face the challenges of future industry?

15

%
Not sure
10%
Yes
90%
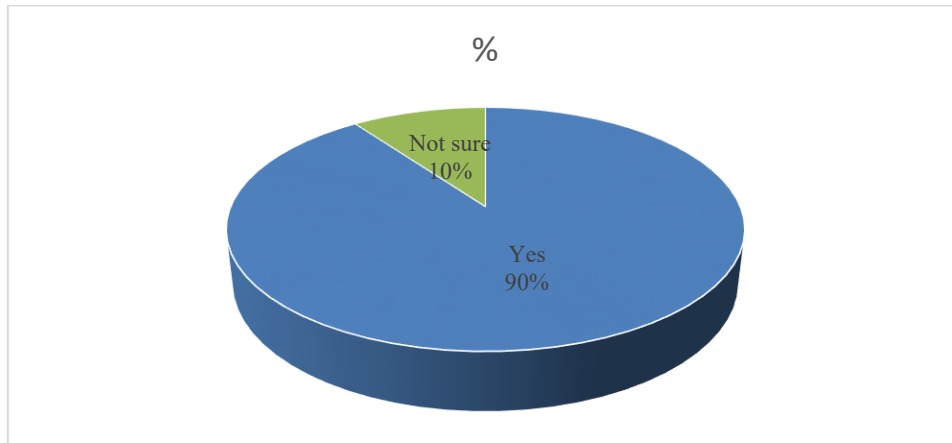
5. Conclusion

Rapidly changing technology has led to the emergence of a skill gap. Ultimately, the students' ability to continuously learn and adapt will determine the extent to which they thrive in today's turbulent times. The extent to which they are able to do this will have an impact not only on who they are today but also on who they can become tomorrow. They also need to adapt and renovate on the lines they think about strategy and implementation. The old school set the goal – plan – execute the approved plan doesn't work anymore. Therefore, a 'context-mindful' framework that embraces learning agility concept should be adopted.

6. References

[1] The Manufacturer, 2017. *Annual Manufacturing Report 2017.* Available at: https://www.themanufacturer.com/wp-content/uploads/2017/01/Annual-Manufacturing-Report-2017.pdf

[2]Lortie, D. *Schoolteacher: a sociological study*. Chicago: University of Chicago Press, 2002.

[3] Manpower, 2015 Talent Shortage Survey. Accessed 15 January 2018. Retrieved from: http://www.manpowergroup.co.uk/wp- content/uploads/2015/06/2015_TalentShortageSurvey_FINAL_lores.pdf

[4] S.Y. Tan, D. Al-Jumeily, J. Mustafina, A. Hussain, A. Broderick, H. Forsyth (2018) Rethinking Our Education To Face The New Industry Era, *EDULEARN18 Proceedings*, pp. 6562-6571.

[5] The Telegraph, Skills shortages at 'critical levels' risking UK growth, research claims Accessed 15 January 2018. Retrieved from: http://www.telegraph.co.uk/business/2018/01/10/skills-   shortages-critical-levels-risking-uk-growth-research/

[6] World Economic Forum, The future of education, according to experts at Davos. Accessed 15 January 2018. Retrieved from: https://www.weforum.org/agenda/2018/01/top-quotes-from- davos-on-the-future-of-education/

[7] Michael Lombardo and Robert Eichinger, "High potentials as high learners," *Human Resource Management* 39, no. 4 (2000): 322.

[8] D. Scott DeRue, Susan J. Ashford, and Christopher G. Myers, "Learning agility: In search of conceptual clarity and theoretical grounding," Industrial and Organizational Psychology 5, no. 3 (2012): 274.

[9] Burke and Smith, "Burke Learning Agility Technical Report: A Guide for Learning about Learning Agility," 12.

[10]Mitchinson, Adam & Morris, Robert. (2012). *Learning About Learning Agility*. Center for Creative Leadership White Paper.

11]S. Y. Tan, A. Hussain, J. Mustafina, A. J. Aljaaf and M. Alloghani, "A Perspective on Education to Support Industry 4.0: A Qualitative Case Study in UK," *2019 12th International Conference on Developments in eSystems Engineering (DeSE)*, 2019, pp. 215-220, doi: 10.1109/DeSE.2019.00048.

[12] Hevner, A.R., March, S.T., Park, J., and Ram, S., "Design Science in Information Systems Research", *MIS Quarterly 28*, 1, 2004, pp. 75–105.

[13] Peffers, K., Tuunanen, T., Rothenberger, M.A., and Chatterjee, S., "A Design Science Research Methodology for Information Systems Research", Journal of Management Information Systems 24, 3, 2007, pp. 45–77.

Pedro Freitas

Postgraduate Researcher

School of Engineering

Impact of RTN and Variability on RRAM-Based Neural Network

P. Freitas, Z. Chai, *W. Zhang, J. F. Zhang, J. Marsland

Department of Electronics and Electrical Engineering, Liverpool John Moores University, Liverpool L3 3AF, UK

*Corresponding author, email: w.zhang@ljmu.ac.uk

Abstract

Resistive switching memory devices can be categorized into filamentary RRAM or non-filamentary RRAM depending on the switching mechanisms. Both types of RRAM devices have been studied as novel synaptic devices in hardware neural networks. In this work, we analyze the amplitude of Random Telegraph Noise (RTN) and program-induced variabilities in both TaO_X/Ta_2O_5 filamentary and TiO_2/a-Si (a-VMCO) non-filamentary RRAM devices and evaluate their impact on the pattern recognition accuracy of neural networks. It is revealed that the non-filamentary RRAM has a tighter RTN amplitude distribution than its filamentary counterpart, and also has much lower programed-induced variability, which lead to much smaller impact on the recognition accuracy, making it a promising candidate in synaptic application.

1. Introduction

Oxide based resistive switching memory devices (RRAM) has emerged as an attractive candidate not only for the next-generation emerging memory technology [1-2], but also as synapses in large-scale artificial neural networks (ANNs) due to its natural synaptic response, simple structure, low energy consumption, and CMOS-compatible 3D integration potential [1]. There are mainly two types of transition-metal-oxide (TMO) based resistive switching devices (RRAM): the conductive filamentary type (CF) that can be implemented with a range of materials, for example, HfO_2 and Ta_2O_5 [2], etc.; and the non-filamentary type (NCF) such as TiO_2/a-Si a-VMCO [3].

In filamentary RRAM devices, variable resistance is induced by repeatable rupture and restoration of a conductive filament (CF) of nanometer scale. The large variations in read current distribution at high resistance state (HRS) is a major concern, as it deteriorates the resistive switching window and causes endurance and retention problems. This has been attributed to defects movement into/out of the constriction of the filament where only a few defects exist. The conductance of individual defect in the constriction has significant impact on the overall resistance levels, and the stochastic nature of individual defect causes large resistance variability and large read instability [4]. Non-filamentary RRAM (NCF) devices have been proposed to overcome the above problems, in which the resistance switching is controlled through the uniform modulation of the defect profile [3]. The a-VMCO RRAM device consists of two layers, in which TiO_2 serves as the switching layer and amorphous-Si as the barrier layer. The non-filamentary switching behavior is demonstrated as its resistance is inversely proportional to the area at both HRS and LRS, and the resistance distributions at both HRS and LRS in a-VMCO RRAM show smaller variations [3, 5].

Random Telegraph Noise (RTN) is the current fluctuation between discrete levels caused by electron trapping and de-trapping in defects. RTN has become a critical issue in nanoscale semiconductor devices where the impact of a single defect becomes significant [6, 7, 8]. As RRAM devices can be scaled down below 10 nm [2], RTN can significantly reduce the memory window and cause read errors in RRAM devices. It is therefore essential to evaluate the impact of RTN disturbance on the performance of RRAM-based synaptic arrays. Program-induced conductance variability in both filamentary and non-filamentary RRAM devices also need to be evaluated in synaptic applications.

In this work, we analyze the amplitude distributions of RTN and program-induced variability in both Ta_2O_5 CF RRAM and TiO_2/a-Si (a-VMCO) NCF RRAM devices. The experimental results are used to simulate their impact on the synapse arrays in a trained artificial neural network. It is revealed that the NCF RRAM has a tighter RTN amplitude distribution and smaller program-induced variability than its filamentary counterpart, leading to much less impact on pattern recognition accuracy and making it a promising candidate as synapse in neural network applications.

2. Devices and Experiments

Both types of RRAM devices were fabricated in a cross- point structure with the size of 75 nm × 75 nm and show bipolar switching characteristics (Fig. 1(a) and (b)). The Ta_2O_5 device consists of a TiN/4nm stoichiometric Ta_2O_5/20nm nonstoichiometric TaOx/10nm TaN/TiN stack (inset of Fig. 1 (a)). The a-VMCO device has a stack of TiN/8nm amorphous-Si/8nm anatase TiO_2/TiN structure (inset of Fig. 1(b)). The detailed process parameters can be found in refs. [5,9]. All electrical tests were carried out with a Keysight B1500A analyzer. Analogue resistance levels are obtained in both devices, between 25 kΩ and 200 kΩ for Ta_2O_5, and

between 1 MΩ and 7.5 MΩ for aVMCO, by incrementing the program pulse number and amplitude. The read-out is at 0.1V and 3V for Ta_2O_5 and aVMCO devices, respectively, by a read pulse width of 100 us. RTN measurement is then carried out at each R level at the read-out voltage, with a sampling time of 2 ms/point and 10,000 sampling points per resistance level for a RTN measurement period of 20 s. A 3-layer ANN was simulated using Matlab. The neural network was trained and tested with the MNIST handwritten digit database. Out of the total 60,000 images, 50,000 were used for training and the remaining 10,000 images unseen during training were used for testing.
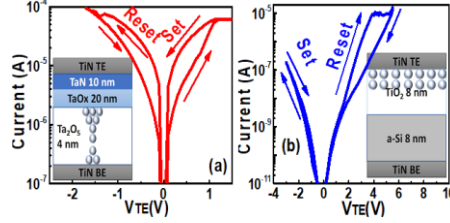
Fig. 1. I-V switching curves of (a) Ta_2O_5 and (b) aVMCO devices; The insets are the schematics of the corresponding structures and the switching mechanism: the restore/rupture of a conductive filament (CF) or the areal modulation of defect distribution inside the oxide (NCF).

3. Results and discussions

3.1 RTN signals in CF and NCF RRAM devices

As shown in Fig. 2(a) and (b), the maximum relative RTN amplitude, $\Delta I/I_{read}$, can be as high as ~300% in the filamentary Ta_2O_5 RRAM device, but only ~10% in the non-filamentary aVMCO. Their CDF distribution plots measured at 8 selected resistance levels are shown in Fig. 2 (c) and (d), respectively. RTN amplitude in Ta_2O_5 device spreads widely from 0.1% to 300%, whilst it is only from 1% to 10% in aVMCO. For both devices, the RTN amplitude follows the lognormal distribution. Moreover, RTN in Ta_2O_5 device has a much higher occurrence rate than in aVMCO device (not shown). The parameters of the distributions are extracted and shown in Fig. 2e & 2f, which will be used in the simulation.

This significant difference in RTN amplitude distribution and occurrence rate can be attributed to the different switching mechanisms, as shown in the insets in Fig.1: in the CF Ta_2O_5 device, the resistance switching is caused by the rupture and restoration of a conductive filament. After the reset, there are only a few defects in the constriction of the CF, and each of them is critical in current conduction, so that its trapping / detrapping leads to large RTN, and hence the higher the resistance level, the larger the RTN amplitude. In the NCF aVMCO device, resistance switching is caused by the uniform modulation of defect distribution. Resistance becomes higher when the "defect-less" region is uniformly widened. A single defect has limited contribution in conduction, hence the much smaller RTN amplitude, and much smaller occurrence rate (not shown), and the amplitude is also only slightly larger at higher resistance levels.
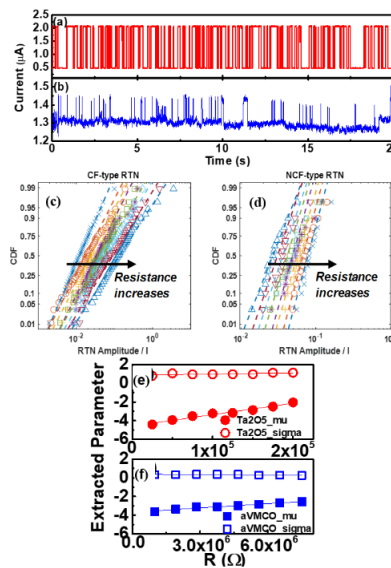

Fig. 2. (a-b) Examples of largest RTN signal in (a) Ta_2O_5 and (b) a-VMCO devices. The relative RTN amplitude can be as high as ~300% for Ta_2O_5 device, but only ~10% for a-VMCO. (c-d) CDF of relative RTN amplitude in (c) Ta_2O_5 and (d) a-VMCO devices, respectively, both following the lognormal distribution. (e-f) Extracted parameters of lognormal RTN amplitude distribution in both devices.

19

3.2 Program-Induced Variability in CF and NCF RRAM devices

The program-induced variability is defined as the relative variation at a target conductance level, i.e. $\Delta G/G$ induced by the programming. In Fig. 3a, four curves programmed at different constant pulse amplitudes in an NCF aVMCO RRAM device are shown as an example, where the typical exponential program kinetics are observed. A linear program approximation can be achieved in a small range on each curve, which is similar to the small signal approximation in AC circuit analysis. By applying a number of smaller identical pulses in each range and incrementing the bias in consecutive ranges, a much improved linearity in the program kinetics can be achieved during both set and reset operations, as shown in **Fig. 3b**.

The program-induced variability obtained in CF and NF devices with the linear response are compared in Fig. 3c and 3d. The program-induced variability in CF device has a wider distribution, leading to much larger variability than that in the NF device. In both devices, the distributions of the relative conductance variability are largely independent of the conductance levels. This allows the use of the observed distribution function to reproduce the variability distribution at any target conductance levels in simulation. which will be demonstrated later.
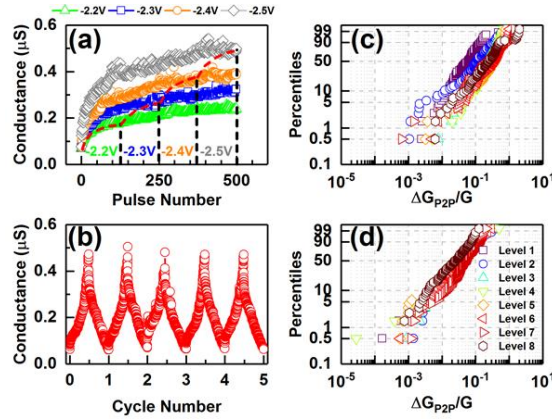

Fig. 3. (a) Illustration of the program kinetics in an NCF RRAM. (b) Linear response can be achieved by applying a number of smaller identical pulses in each range and incrementing the bias in consecutive ranges. (c) Distribution of the program-induced variability at 8 selected conductance levels across the memory window in CF RRAM and (d) in NCF RRAM.

3.3 Impact of RTN on NN accuracy

The impact of RTN on the pattern recognition accuracy of RRAM based synaptic neural network is analysed first. The neural network consists of 3 layers with 30 neurons in the hidden layer, as shown in Fig. 4(a). The neural network is trained with the mini-batch gradient descent backpropagation algorithm. The accuracy after training without and with the RTN induced disturbance in both CF and NCF RRAM are statistically shown in Fig. 4(b). The change of weights in one of these procedures is visualized in Fig. 4(c), in which the weights are shown in (1) without disturbance, (2) after the CF disturbance, and (3) after the NCF disturbance. The weight differences are shown in (4) after CF disturbance and (5) after NCF disturbance.
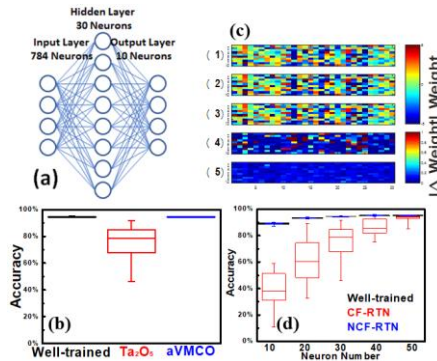

Fig. 4. (a) Schematic of the pattern recognition ANN. (b) Statistical accuracy in 50 training-disturbance procedures: Accuracy is hardly affected with the NCF disturbance, while with the CF disturbance the accuracy is severely deteriorated. (c) Visualization of weights: (1) directly after training; (2) with CF RTN disturbance; (3) with NCF RTN disturbance; (4-5) their differences to case (1), respectively. (d) Accuracy of ANN with different neuron number without and with CF and NCF RTN disturbance. ANN with NCF devices needs fewer neurons/synapse and have better accuracy.

As shown in Fig. 4(b), after the CF RTN disturbance, the average accuracy drops to ~75% with a wide repeatability distribution and its lowest is less than 50%, while after the NCF disturbance the accuracy drops negligibly only to 94% with a similar repeatability to that without disturbance, as can also be clearly seen in the weight differences shown in Fig. 4(c). This proves that the non-filamentary RRAM device has a strong advantage compared to the

conventional filamentary devices in the synaptic application, due to its small RTN amplitude and low RTN occurrence rate. Furthermore, as shown in Fig.4(d), the neural network with NCF synaptic devices maintains a high accuracy of ~90% even when only 10 neurons are used in the hidden layer, whilst the accuracy drops sharply with the CF devices. NCF synaptic devices allows a much smaller ANN to achieve better accuracy due to its robust RTN resilience, therefore.

3.4 Impact of program-induced variability on NN accuracy

The impact of program-induced variability on the pattern recognition accuracy in CF and NCF RRAM devices are compared in Fig. 5. The accuracy loss caused by program-induced variability in non-filamentary RRAM device is significantly smaller than that in the filamentary RRAM device, thanks to the much smaller variability. RTN-induced accuracy loss is also shown for comparison, and it is even larger than that induced by the program-induced variability. The overall pattern recognition accuracy is limited by RTN in the NCF devices. Program-induced variability in CF RRAM and RTN induced variability in NCF RRAM are the most significant sources responsible for accuracy loss, respectively.
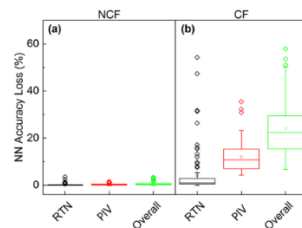

Fig. 5. Comparison of the NN accuracy loss caused by different sources of variability of (a) NCF RRAM and (b) CF RRAM, including RTN and program-induced variability (PIV) programmed with linear (LR) kinetics. NF device shows much lower variability-induced accuracy loss compared with its CF counterpart. RTN in NCF RRAM and program-induced variability in CF RRAM are the dominant sources of accuracy loss.

The difference in program-induced variability in NF and CF RRAMs can also be attributed to their different switching mechanisms. The area-dependent resistance in non-filamentary devices supports that the resistance is uniformly modulated across the lateral device area during the switching and individual defect movements are averaged out, leading to the much smaller variability in device conductance. In contrast, the area-independent resistance in conductive filamentary devices supports that the switching is controlled by the rupture and restoration of one local filament between the two electrodes. where individual defects play a significant role in the conductance change of the CF device. This translates into not only a more pronounced RTN amplitude with wider distribution, but also in higher program-induced variability. Non-filamentary RRAM demonstrates far better immunity to variability and hence better inference accuracy in HNN applications, therefore.

3.5 Conclusions

In this paper, two different variability sources are statistically measured and evaluated at different conductance levels across the memory window in both conductive-filamentary and non-filamentary RRAM devices. Based on the statistical distributions of the program-induced variability and RTN in both NF and CF RRAM devices, their impact on the pattern recognition accuracy of a RRAM-based 3-layer feedforward HNN are simulated and compared. It is revealed that NF device shows much lower variability and accuracy loss than its CF counterpart. RTN remains a major variability source in both devices. A comparison between the NF and CF switching mechanisms can explain the differences in the variability and their distributions.

Acknowledgments

References

[1] Wong et al, IEEE proc., 2012.
[2] Govoreanu et al, IEDM, 2011.
[3] Govoreanu, et al, VLSI Symp. Tech. Dig., 2015
[4] Degraeve et al, VLSI, 2012.
[5] Ma, et al, IEDM 2016.
[6] Chai, et al, VLSI Symp. Tech. Dig., 2016
[7] Chai, et al, IEEE, TED, 2017
[8] Kirton et al, Advances in Physics, 1989.
[9] Chai et al, IEEE EDL, 39 :955-958, 2018.

Robert Poole-McKenzie

Postgraduate Researcher

Astrophysics Research Institute

Implications for dark matter direct detection searches using the ARTEMIS simulations

R Poole-McKenzie, A S Font, B Boxer, I G McCarthy, S. Burdin, S Stafford & S Brown

[1]2.24, Astrophysics Research Institute, 146 Brownlow Hill, Liverpool, L3 5RF
[2]The Oliver Lodge, University of Liverpool, Oxford St, Liverpool, L69 7ZE
r.poolemckenzie@2013.ljmu.ac.uk

Abstract: The direct detection of dark matter (DM) relies significantly on its local velocity distribution and density. An accurate model of local DM properties is essential to place reliable constraints on DM particle cross-sections. Current methods adopt the Standard Halo Model (SHM) which assumes a simple Maxwellian distribution of local DM velocities and a fixed value for the local DM density. We investigate the local DM velocity distribution and density using Milky Way mass-like galaxies generated from new, high-resolution cosmological zoom simulations called ARTEMIS. The halos used in this work provide a more representative sample of Milky Way mass-like disk galaxies than previous studies. Our results show the velocity distribution in the local neighbourhood varies significantly from halo-to-halo and the mean of the distributions is well described using a simple Maxwellian distribution in the hydrodynamic case. We obtain a local DM density of 0.23-0.47 GeVcm^{-3}. For the DM-only case we find that the local velocity distribution is less well described using a Maxwellian and the peak velocity is smaller. We concluded that the SHM is justified to use a Maxwellian distribution, however the variation on local DM v_0 and ρ_0 seen from halo-to-halo increase the uncertainty when determining the WIMP cross-sections.

1. Introduction

1.1 Dark matter and the WIMP

Dark matter (DM) is the most influential component of matter in the Universe and plays a vital role in the formation of large-scale and galactic structures. The evidence for DM is strong, with flat rotation curves from spiral galaxies [1, 2], cosmic microwave background anisotropies [3], velocity dispersions in galaxy clusters [4] and masses obtained from gravitational lensing [5] all suggesting the existence of a new, non-baryonic particle. However, identifying the exact nature of DM remains a mystery. Very little is known about DM as a particle, although it must be consistent with several observational constraints [6]. Particle physics has suggested numerous particle candidates beyond that of the Standard Model (SM), with the most compelling evidence favouring that of a new electromagnetically neutral, non-baryonic particle - the Weakly Interacting Massive Particle (WIMP) [7]. The existence of the WIMP or any other particle beyond the SM will not be verified until a signal is clearly identified via indirect or direct detection experiments or in particle accelerators.

1.2 Direct detection

The observationally confirmed presence of a DM halo in our Galaxy provides an interesting source of investigation for DM particle searches. This work will focus on direct detection experiments with numerous experiments having played an important role in this attempt to directly detect DM in the form of WIMPs via their elastic scattering off of nuclei [8]. The interaction rate from the DM interactions relies significantly on the local velocity distribution and the local DM density. An accurate model of the local DM velocity distribution is essential to place improved constraints on the DM particle properties. Current direct detection experiments adopt an isothermal and isotropic theory known as the Standard Halo Model (SHM). The SHM assumes that the velocity distribution is Maxwellian, with a peak speed of 220 kms^{-1} and uses a constant value of $\rho_\chi = 0.3$ GeVcm^{-3}. However, the this may not be the case.

2. Methodology

We investigate the local DM velocity distribution of 42 Milky Way mass-like halos generated from new, high-resolution, hydrodynamical cosmological simulations called ARTEMIS [9]. The new simulations have the advantage of increased resolution, which is a result of using the "zoom-in" technique, where a halo is identified in a lower resolution simulation, and then re-simulated. These simulations have been implemented with (hydrodynamic) and without baryonic physics (DM-only – DMO).

Throughout this study we adopt a coordinate system that is in the rest frame of the galaxy. This is achieved by aligning the halo with the principle axis of the angular momentum calculated within the stellar disks inner 20kpc. Our new reference system has the origin at the galactic centre, x and y are in the plane of the stellar

disk and z is perpendicular to the stellar disk. For the halos in the DMO simulations, we use the alignment coefficients from the matched hydrodynamic halos to orientate the coordinates.

We define the Solar neighbourhood (local) region as a cylindrical shell with a radial distance 4% of $R_{200} \pm 1$ kpc and 1.5 kpc either side of the galactic plane. We select 4% as this is the distance of the Sun from the Galactic centre with respect to the Milky Way's virial radius, $R_{200} \approx 210$ kpc [10]. The newly defined local region contains a total of 10,611- 21,144 DM particles for the hydrodynamic simulations and 6,889 - 17,980 for the DMO simulation.

3. Results

3.1 Local dark matter densities

The volume averaged local DM densities are in the range of 0.23 - 0.47 GeVcm^{-3} for the halos in our hydrodynamic simulations and 0.15 - 0.38 GeVcm^{-3} for the DMO simulations. The difference in densities between the hydrodynamic and DMO simulations is as expected, with the dissipative baryons deepening the potential well at the centre of the halos, increasing the number of particles in the inner regions and hence increasing the regions density.
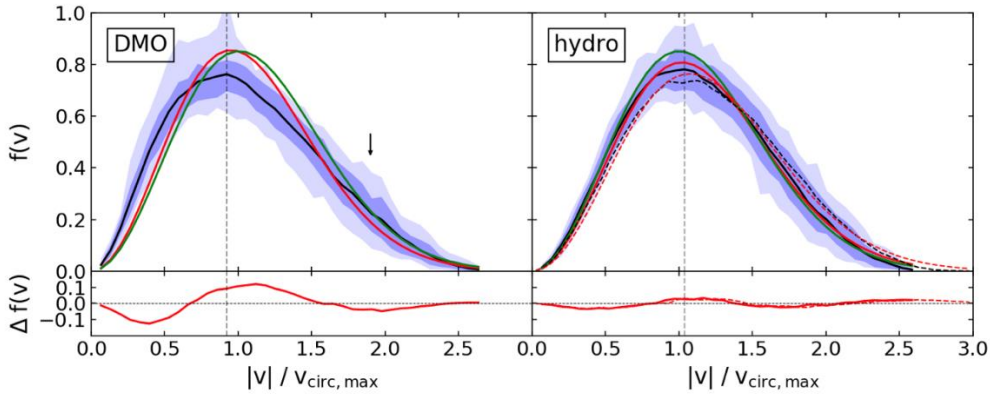

Figure 1 - Dark matter velocity modulus distributions in the rest frame of the galaxy, normalised by the maximum rotational velocity, V$_{max}$. The solid black line represents the mean of velocity modulus distributions for the DMO (left) and hydrodynamic (right) simulations. The solid red line represents the mean of the best fitting Maxwellian distributions. The dark and light blue contours enclose 68% and 95% of the velocity distribution from all halos. The lower panels show the residuals between the mean distribution of the halos and the mean Maxwellian fit.

3.2 Local dark matter velocities

We analyse the velocity distributions generated from our hydrodynamic and DMO simulations for all of our selected halos and compare them with the Maxwellian hypothesis. Using the aligned halos from both the hydrodynamic and DMO simulations we are able to calculate the local velocity modulus distribution and determine the distribution of local velocities (figure 1).

Figure 1 shows the mean local DM velocity modulus distribution in the rest frame of the galaxy for all halos in the hydrodynamic and DMO simulations. All halos in both sets of simulations have been fitted with a Maxwellian distribution. We find that the hydrodynamic case is reasonably well described by a Maxwellian distribution, with a slight deviation at very high velocities. In contrast, the DMO case is poorly described by a Maxwellian, with large deviations seen at both low velocities and in the peak of the distribution. We also observe significant halo-to-halo variation in the distributions for both cases. The mean local velocity distribution has a peak velocity of $v_0 = 179$ kms^{-1} and $v_0 = 160$ kms^{-1}, for the hydrodynamic and DMO simulations respectively. The higher peak velocity in the hydrodynamic simulations can be attributed to the effect of the baryons deepening the potential well of the halo, causing the particles to travel at higher velocities.
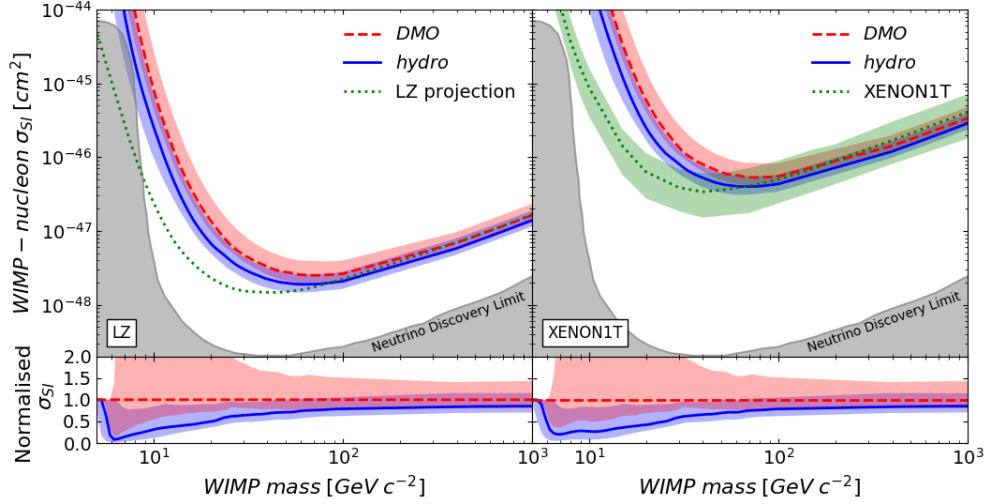
Figure 2 – The exclusion limits for the ARTEMIS halos with XENON1T (right) and LZ (left) parameters. The mean upper-limits are shown as red and blue lines for the DMO and hydrodynamic case, respectively. The contours enclose 68% of all the individual exclusion limits for the 42 halos. The green dotted line shows the experimental predictions from XENON1T and LZ, which assume the Standard Halo Model.

3.3 Implications for direct detection

As mentioned previously, the limits placed on the WIMP-nucleon cross-section are dependent on several local DM properties. In addition to these, the limits rely on experimental parameters such as the detectors material and mass, as well as the number of days the experiment runs for (i.e. live-days). Currently the most sensitive result and most constraining value on the WIMP-nucleon cross-section has be determined by the XENON1T direct detection experiment [11], with future experiments like LZ aiming to improve the sensitivity [12].

Figure 2 shows our predicted WIMP interaction cross-section constraints, assuming a Maxwellian distribution of velocities. We apply the local DM densities, local peak velocities and escape velocities of the halos from our simulations into our interaction cross-section calculations, as well as the experimental parameters used by XENON1T and LZ. We also provide results for the DMO case, which demonstrates the effect of baryons on the results from direct detection experiments. We also compare the XENON1T result with the. LZ projection.

We find that the hydrodynamic case places a lower upper limit on the WIMP interaction cross-section than the DMO case. This is caused by the lower local DM densities in the DMO simulation, a lower density requires a larger cross-section to produce the same interaction rate. The variation seen the local velocity distributions propagates through to the cross-section results, increasing the uncertainty on upper limits. The differences seen between our results and the experimental data at low WIMP masses can be attributed to the lower escape velocities of our simulations than that of the Milky Ways. The variation seen in the hydrodynamic case places a lower upper-limit on the WIMP-nucleon cross-section, constraining the WIMPs physical properties further than experimental predictions.

4. Summary

We have used a new suit of zoomed cosmological simulations from a modified EAGLE code to produce Milky Way-like halos in order to study the local DM density and velocity distributions, to understand the implications for direct detection. The main points from this work are summarised below:

- The local DM velocity distribution of the hydrodynamic simulations are well defined by a Maxwellian, however the DMO simulations are poorly described using a Maxwellian.
- The impact of the baryons in the hydrodynamic simulations drives a shift of the peak velocity to higher velocities when compared to the DMO case.
- The significant halo-to-halo variation in the velocity distributions caused by the range of densities and peak velocities in the simulations adds additional uncertainty to the exclusion limits for direct detection experiments.
- The variation in the hydrodynamic WIMP-nucleon cross-section shows that the experimental predictions may be lower than expected when ranges of densities and velocities are considered.

5. References

[1] V. C. Rubin, N. Thonnard and W. K. Ford, Jr., Extended rotation curves of high-luminosity spiral galaxies. I - The angle between the rotation axis of the nucleus and the outer disk of NGC 3672, 217 (1977) L1.

[2] P. Salucci, A. Lapi, C. Tonini, G. Gentile, I. Yegorova and U. Klein, The universal rotation curve of spiral galaxies - II. The dark matter distribution out to the virial radius, 378 (2007) 41.

[3] M. White, D. Scott and J. Silk, Anisotropies in the Cosmic Microwave Background, 32 (1994) 319.

[4] F. Zwicky, On the Masses of Nebulae and of Clusters of Nebulae, 86 (1937) 217.

[5] E. Aubourg, P. Bareyre, S. Bréhin, M. Gros, M. Lachièze-Rey, B. Laurent et al., Evidence for gravitational microlensing by dark objects in the Galactic halo, 365 (1993) 623.

[6] Arcadi, G., et al. (2018). The waning of the WIMP? A review of models, searches, and constraints. *The European Physical Journal C*, *78*(3), 203.

[7] Steigman, G., & Turner, M. S. (1985). Cosmological constraints on the properties of weakly interacting massive particles. *Nuclear Physics B*, *253*, 375-386.

[8] Goodman, M. W., & Witten, E. (1985). Detectability of certain dark-matter candidates. *Physical Review D*, *31*(12), 3059.

[9] Font, A. S., McCarthy, I. G., Poole-Mckenzie, R., Stafford, S. G., Brown, S. T., Schaye, J., ... & Schaller, M. (2020). The ARTEMIS simulations: stellar haloes of Milky Way-mass galaxies. *Monthly Notices of the Royal Astronomical Society*, *498*(2), 1765-1785.

[10] J. I. Read, The local dark matter density, J. Phys. G: Nucl. Part. Phys. 41 (2014) 063101.

[11] E. Aprile, J. Aalbers, F. Agostini, M. Alfonsi, F. D. Amaro, M. Anthony et al., First Dark Matter Search Results from the XENON1T Experiment, Phys. Rev. Lett. 119 (2017) 181301.

[12] Akerib, D. S., et al. "Projected WIMP sensitivity of the LUX-ZEPLIN dark matter experiment." *Physical Review D* 101.5 (2020): 052002.

Joaquin García de la Cruz

Postgraduate Researcher

Astrophysics Research Institute

On the flaring of thick discs of galaxies: insights from simulations

J. García de la Cruz

Astrophysics Research Institute, 146 Brownlow Hill, Liverpool, L3 5RF

E-mail address: j.garciadelacruz@2017.ljmu.ac.uk

Abstract. Using simulated galaxies in their cosmological context, we analyse how the flaring of mono-age populations (MAPs) influences the flaring and the age structure of geometrically defined thick discs. We also explore under which circumstances the geometric thin and thick discs are meaningfully distinct components or are part of a single continuous structure as in the Milky Way. We find that flat thick discs are created when MAPs barely flare or have low surface density at the radius where they start flaring. When looking at the vertical distribution of MAPs, these galaxies show a continuous thin/thick structure. They also have radial age gradients and tend to have quiescent merger histories. Those characteristics are consistent with what is observed in the Milky Way. Flared thick discs, on the other hand, are created when the MAPs that flare have a high surface density at the radius where they start flaring. The thick discs' scale-heights can either be dominated by multiple MAPs or just a few, depending on the mass and scale-height distribution of the MAPs. In a large fraction of these galaxies, thin and thick discs are clearly distinct structures. Finally, flared thick discs have diverse radial age gradients and merger histories, with galaxies that are more massive or that have undergone massive mergers showing flatter age radial gradients in their thick disc.

Key words: galaxies: structure – galaxies: spiral – galaxies: interactions – galaxies: formation – galaxies: evolution – methods: numerical

1. Introduction

Thick discs were first discovered in external galaxies by Tsikoudi (1979) and Burstein (1979), and later on in the Milky Way by Gilmore & Reid (1983). Since then, they have been shown to be present in the majority of disc galaxies (Dalcanton & Bernstein 2002; Yoachim & Dalcanton 2006; Comerón et al. 2018). There are many ways to define thick discs. The geometrical thick disc refers to a second exponential component in either a disc's vertical light profile (e.g., Tsikoudi 1979), or stellar density (Juric et al. 2008). This definition can be used both for external galaxies and the Milky Way, for this reason, we will use a geometric definition as it can be applied to all galaxies. Among other thick disc properties, one this work focuses on is the global shape of the disc, i.e. the possible variations of scale-height with radius. Studies on large samples of galaxies (e.g., Yoachim & Dalcanton 2006; Comerón et al. 2011, 2012, 2014, 2018) concluded that the vast majority of thick discs in external galaxies have a constant scale-height with radius. The studies which found only flat thick discs, however, either show one averaged scale-height for the whole thick disc (Yoachim & Dalcanton 2006), or describe the disc with only a few radial bins (Comerón et al. 2011, 2012, 2014, 2018), making it difficult to observe variations in the scale-heights with galactic radius. However, other works have also found thick discs with a significant amount of flaring (Narayan & Jog 2002; Kasparova et al. 2016; Sarkar & Jog 2019; Kasparova et al. 2020), and Rich et al. (2019) found boxy shaped isophotes in the outer disc of some edge-on galaxies, which indicate strong disc flaring (Mosenkov et al. 2020). In the Milky Way, although flaring in the inner disc (~11 kpc) is highly disfavoured (Mateu & Katherina Vivas 2018), the existence of thick disc flaring in the outskirts (Robin et al. 2014a; Mateu & Katherina Vivas 2018; López-Corredoira et al. 2018; Thomas et al.2018), and the amplitude of the effect (Reylé et al. 2009; Polido et al. 2013; Kalberla et al. 2014; López-Corredoira & Molgó 2014; Amôres et al. 2017) are still a matter of debate. In any case, there is increasing evidence that thick discs might be more diverse than previously thought in terms of global shape and flaring.

Similarly, the age structures created by the stellar populations in thick discs are also showing more diversity in recent studies than previously thought. Some works using broadband photometry (e.g., Dalcanton & Bernstein 2002; Seth et al. 2005; Mould 2005) and spectroscopy (Yoachim & Dalcanton 2008; Comerón et al. 2015,2016) helped establish the classical view of thick discs as red, old, and metal poor components. However, more recent works suggest that thick discs are diverse and have complex age structures. Kasparova et al. (2016) analysed spectroscopically three edge-on galaxies and found that while one has a very old thick disc (~10 Gyr), the other two have intermediate age (~5 Gyr) stars in their thick discs. In the Fornax cluster, Pinna et al. (2019a,b) found that in FCC 170 (NGC 1381), FCC153 and FCC 177, the thick discs are very old, but host complex populations. In the Milky Way, the geometrically thick disc is made of old stars in the solar neighbourhood and the inner disc, but shows a strong radial age gradient: between galactocentric radii of 6 and 12kpc, the mean age of red clump stars in the thick disc drops from ~9 to ~5 Gyr (Martig et al. 2016, see also Ness et al. 2016; Xiang et al. 2017; Feuillet et al. 2019). Therefore, a picture is emerging where thick discs can host complex stellar populations, have different age structures, and also possibly different relationships with the thin discs.

The age structure of thick discs is also connected to the important question of their relationship to thin discs: are thin and thick discs clearly distinct components, and is the separation meaningful? Bovy et al. (2012a) have then

shown that the transition from thin to thick disc corresponds to a continuum of stellar populations, and that the Milky Way's thick disc is not a distinct component. Whether the Milky Way is a unique case or not is still unknown, but what is most likely is that there exists a variety of disc structures. Ultimately, the age structure of thick discs and the thin/thick disc dichotomy must be linked to the formation process of galactic discs.

Thick discs have been proposed to be a natural consequence of ΛCDM (Read et al. 2008). Yet, their exact origin is still a matter of debate. Bournaud et al. (2009) proposed that flat thick discs could form through a clumpy and turbulent phase in the evolution of galaxies at early times. Observations of flat thick discs favoured this scenario, but it remained unknown why mergers (an inevitable consequence of ΛCDM) did not produce disc flaring as seen in the simulations (Kazantzidis et al. 2008, 2009; Qu et al. 2011; Moetazedian & Just2016). Minchev et al. (2015) proposed a solution for this conundrum, showing that a flat thick disc can be recovered by superposing several stellar mono-age populations, MAPs, with different levels of flaring and radial density profiles. This same effect has been found in other sets of simulations as well, like LATTE (Ma et al. 2017), AURIGA (Grand et al. 2014), NIHAOUHD (Buck 2020), and VINTERGATAN (Agertz et al. 2020), and in observations of the Milky Way (Xiang et al. 2018).

In this paper, we expand on the work of Minchev et al. (2015) by studying the structure of discs in the full sample of simulated galaxies presented in Martig et al. (2012). We first present some general properties of the simulated galaxies and their discs, but the main focus of the paper is to explore how much MAPs flare, and what kind of thick disc they create. We pay special attention to three aspects: a) how flaring MAPs can create either a flat or flared thick disc, b) whether those thick discs define a separate structure from the thin disc or not (in terms of their stellar populations), c) and the different kinds of age gradients MAPs create. Finally, we look into the merger histories of our galaxies, and show the connection between mergers and different thick disc properties.

2. Methods

2.1 Simulations

We use a sample of zoom-in numerical re-simulations of galaxies in their cosmological context described in more detail in Martig et al. (2012). The simulation technique consists of two different
stages (see Martig et al. 2009). In the first stage, a dark-matter-only ΛCDM cosmological simulation is run with 512^3 dark matter particles using the adaptive mesh refinement code RAMSES (Teyssier
2002). We identify dark matter haloes with a final mass between 2.7×10^{11} and 2×10^{12} $M_\odot$ that live in isolated environments. Then, merger histories and diffuse dark matter accretion are recorded for
those halos from z = 5 to z = 0, storing the time, mass, velocity, and spin of the satellites.

In the second stage, a new simulation follows the growth of a seed galaxy which evolves from z = 5 to z = 0 using the merger and accretion histories obtained in the first simulation. Each incoming halo is replaced by a galaxy containing stars, gas, and dark matter. This new simulation uses the Particle-Mesh code described by Bournaud & Combes (2002, 2003) with a sticky-particle algorithm
for modelling gas dynamics. The total size of the box is 800 x 800 x 800 kpc, and the spatial resolution is 150 pc. The mass resolution is 1.5×10^4 $M_\odot$ for gas particles and stellar particles formed during the simulation, 7.5×10^4 $M_\odot$ for stellar particles in the initial seed galaxies at z = 5, and 3×10^5 $M_\odot$ for dark matter particles. Star formation obeys a Schmidt-Kennicutt law (Kennicutt 1998), and
energy feedback from supernovae is included. A mass loss scheme is implemented following that of Jungwiert et al. (2001) and used in Martig & Bournaud (2010). A full detailed explanation of the
simulation technique is in Appendix A of Martig et al. (2009).

2.2 The sample

The original sample consists of 33 simulated galaxies presented in Martig et al. (2012) with stellar masses between 10^{10} and 2×10^{11} $M_\odot$, and a large diversity of morphologies and formation histories. Some of the galaxies in the sample have structural features that would vastly complicate our analysis: these are galaxies either undergoing a massive merger at z = 0, or having a polar ring, or presenting a dramatically warped and distorted disc. For that reason, in this work we exclude 6 from the original sample, leaving us with 27 galaxies (see some examples in Fig. 1).
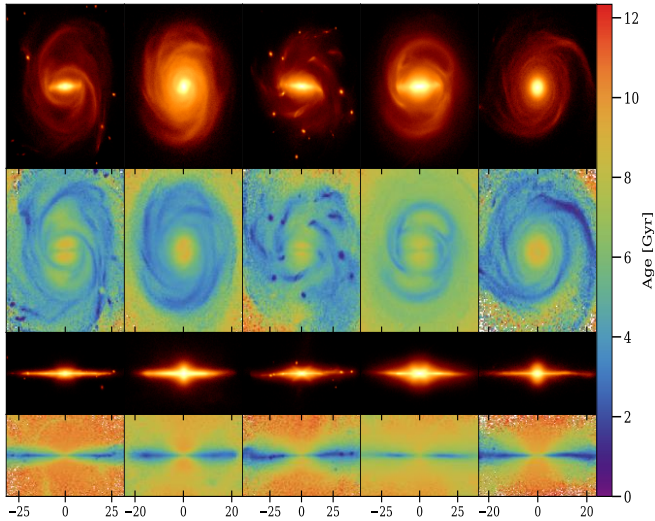
Figure 1. Density and age maps seen face-on and edge-on of five galaxies from

2.3 Scale-height

We first compute a global estimate of the overall disc thickness: we define h_{scale} as the standard deviation of the vertical position of stars located at half the optical radius of the galaxy, R_{25}. To then compute the scale-heights of the global thin and thick disc, we bin the disc stellar particles in cylindrical shells with a width of 2 kpc and a height of $3 \times h_{scale}$ as the standard deviation of the vertical position of stars located at half the optical radius of the galaxy, R_{25}. At each radius, we compute the vertical number density of particles using 20 bins, and fit the profile using a combination of two $sech^2$ functions:

$$N(z) = N_0 \left((1-\alpha)sech^2\left(\frac{z}{h_{thin}}\right) + \alpha sech^2\left(\frac{z}{h_{Thick}}\right) \right) \qquad (1)$$

where N_0 is the stellar number density at the mid-plane, h_{thin} and h_{Thick} correspond to the scale-height of the thin and thick disc respectively, and α is the number density fraction of the thick disc over the global disc. We find that a single $sech^2$ could not describe well the vertical distribution of stars, especially for the thickest discs. To determine the vertical stellar distribution of stars, following Bennett & Bovy (2019), we use a Poisson distribution for the likelihood, which we write as follows:

$$ln\mathcal{L}\left(N_c|N_p\right) = \sum -N_p + N_c \cdot ln\left(N_p\right) - ln(N_c!) \qquad (2)$$

where N_c is the number of stellar particles counted in the bin, N_p is the number of stellar particles predicted by the model, and $N_c!$ is independent of the models and thus ignored for the computation of the likelihood. The fits for the scale-height were obtained using Markov Chain Monte Carlo (MCMC) with the python package emcee (Foreman-Mackey et al. 2013), with 200 walkers and 5000 steps. The walkers start from random positions around the best fit value obtained using the ScyPy routine *curve_fit* (Virtanen et al. 2019). For the priors, we h_{thin} and h_{Thick} take any value from 0 to 15 kpc, α from 0 to 1, and we set N_0 to be positive. The final values we report for each parameter are the median and the 16th to 84th percentiles range of the posterior distribution. An example of the MCMC fits can be seen in Fig. 2. In addition to fits to the thin and thick discs, we also determine the scale-heights of MAPs, for which we split the stellar particles into 0.5 Gyr age bins ranging from 0 to 13 Gyr old, and the same spatial bins as for the fits of the global thin and thick discs. Martig et al. (2014a) showed that a single exponential provides a good fit to the vertical density profile of MAPs, as was also found by Minchev et al. (2015). Nevertheless, since we used a squared hyperbolic secant to fit the thin and thick discs, we used this same function to fit the MAPs in order for both MAP and thin/thick global scaleheights to be comparable. The fits for the MAPs' scale-heights are done in each radial bin, from the galactic centre to R_{25} until eitherthere are fewer than 10 stellar particles inside the bin or the scaleheights are greater than 10 kpc.

3. Discussion

3.1 Mono-age populations and thick disc connection

Non-flaring MAPs will not contribute to the flaring of the thick disc anywhere, rather, they will tend to minimise the flaring of the thick disc especially at those radii where their contribution to the total disc's surface density is more significant. Likewise, flaring MAPs that have a low surface density at the radii they flare, will not contribute either to the flaring of the thick disc. On the contrary, flaring MAPs with a substantial contribution to the total surface density at the radii they flare will drive thick disc flaring. Since the surface density contribution changes with radius for every MAP, the global flaring will be driven by different MAPs at different parts of the disc. In some galaxies, the scale-heights and flaring level of MAPs increase gradually with age. In others, there are gaps between particular MAPs, or quite a few MAPs have roughly the same scale-heights. Martig et al. (2014b) found that these gaps are linked to the galaxy merger history.

3.2 Bimodal vs. continuous structure

On the one hand, a thin/thick disc bimodality scenario is one where the disc has two components with comparable surface densities and each component has only certain MAPs. In g102, the younger MAPs do not flare much and form the thin disc, whereas the older MAPs flare —and have the same scale-heights— and form the thick disc. Therefore, the thin and thick discs are clearly spatially divided and the stellar populations populating them are completely different regarding their age. Also, both disc components have a considerable amount of surface density. On the other hand, a continuum scenario is one where the transition between MAPs forming the thin disc and those of the thick disc is smooth, without clear massive distinct components

Finally, we find 6 galaxies in our sample that we classify as intermediate cases. These galaxies do not have a single gap in their MAPs' scale-heights but a few of them. However, because of the changing surface density with radius, sometimes the global thick disc's scale-heights are above a particular gap and sometimes below depending on radius

3.3 Age gradients

A consequence of the combination of MAPs flaring and dominating the surface density in different disc radii is the creation of age gradients in the radial direction. In this section, we describe the age gradients in our galaxy sample and we explain how the different MAPs' flaring scenarios create radial age gradients

(flat thick discs), the MAP dominating the surface density is changing all the time as a function of radius. This makes the median stellar age decrease with radius. Flared thick discs show a more diverse variety of age gradients. However, because MAPs are more ex-tended in the vertical direction compared to cases 1a and 1b, the thick disc's scale-heights cross through only a few MAPs, which cover a small age range. This, together with how these MAPs' sur-face densities are distributed radially, creates a flat age gradient as a function of thick disc's scale-height.

3.4 Mergers and formation histories

While secular evolution and radial migration can in some cases induce some disc flaring (Minchev et al. 2012a; Martig et al. 2014b), interactions between discs and satellite galaxies are one of the main mechanisms causing flaring. How much flaring is induced depends on multiple factors such as the orbit and mass of the satellite, and the bulge fraction of the main galaxy (Kazantzidis et al. 2008, 2009; Qu et al. 2011; Moetazedian & Just 2016). It is not within the scope of this work to explore meticulously how those different factors produce different effects on disc dynamics and flaring, but we can observe some of their most noticeable effects, and explain some configurations of thick disc, MAPs, and age gradients.

In Fig. 3 we show the age gradient along the thick disc ∇_{age} as a function of the thick disc's scale-height slope ∇_{Thick} colour-coded by the stellar mass of the most massive merger in the last 9 Gyr in the upper panel, and the mass ratio of that merger in the bottom panel. The shape of the points indicates whether the thin and thick disc form a bimodal structure or not as explained in Sec. 3.2. The stellar mass of the satellites is computed right before their first interaction with the disc of the main galaxy. Thus, we are not considering the initial mass of satellites and their disruption as they cross the galactic halo, which is a process that could be potentially altered by numerical resolution (Van Den Bosch et al. 2018). We also refer the reader to Martig et al. (2012, 2014b) for a more detailed discussion of some of the resolution tests that we have performed
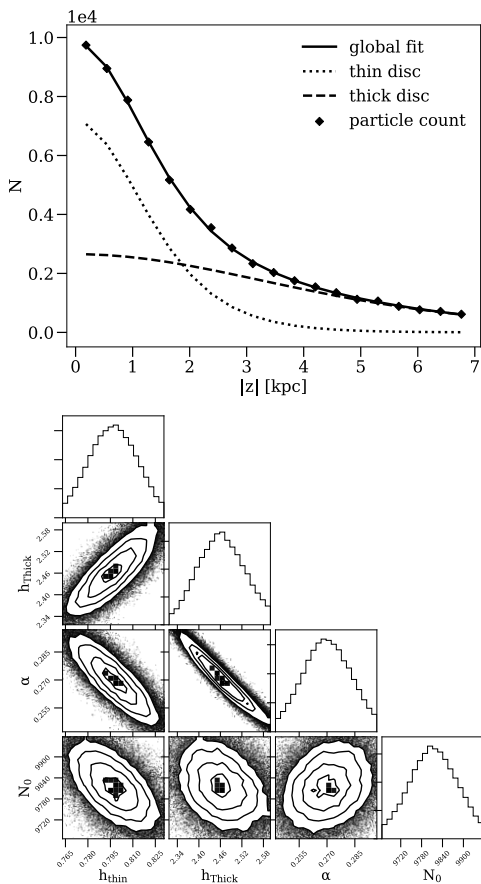

Figure 2. Top: Vertical distribution of number density of stellar particles in black diamonds and the MCMC fit in solid black line. The dotted and dashed line represent the thin and thick disc contribution to the total particle count. The blue range indicates the 16th to 84th percentiles range of the posterior distribution. Bottom: corner plot of the parameter values for the MCMC fit to the vertical number density profile. presented in the upper panel.

We find that galaxies with flat thick discs all had very quiescent merger histories: all of those galaxies (except g106 that had a 1:15 merger around 8 Gyr ago) only have mergers smaller than 1:30 in the last 9 Gyr. Radial age gradients along the disc are a natural consequence of an inside-out disc growing formation scenario. As the disc forms and grows gradually, younger MAPs are born and dominate the density towards the outer regions. For flat thick disc galaxies, which generally have quiescent merger histories, this configuration will remain intact as the MAPs' flaring is either minimal or happens at the radii with low surface density. Therefore, flat thick disc will tend to have a radial age gradient along the disc, which is what we observe in Fig. 3. Flared thick disc galaxies show more diversity. Galaxies

with more massive mergers tend to have flat age gradients (less than –0.1 Gyr/kpc) and also tend to have some degree of flaring (more than 0.02). All the galaxies having merged with satellites more massive than $4.5 \times 10^9\ M_\odot$ show either mild or strong bimodality, although there is no strong correlation between the degree of bimodality and the mass of the satellite. For instance, g59 underwent a massive merger but only shows mild bimodality. This could be due to different factors, like the merger's orbit: exploring this is not within the scope of this paper, and future work will be needed on this matter. The bottom panel of Fig. 3 shows similar results. Most galaxies that underwent mergers with a mass ratio higher than 1:10 seem to have more flared thick discs with flat age gradients. These galaxies also show strong thin/thick disc bimodality. By contrast, we also find galaxies with a quiescent merger history but a flared thick disc and a flat age gradient. For these galaxies, there must be other mechanisms besides mergers causing both the flaring of the thick disc and the flat age gradient. In some of these galaxies, MAPs are born already with some degree of flaring, which has been reported in other cosmological simulations (e.g. Navarro et al. 2018). As for the others, MAPs were born in flatter configuration. The source of flaring for these MAPs can be internal heating mechanisms or ex-ternal agents such flybys or multiple minor mergers throughout the lifetime of the galaxy. However, most galaxies in our sample have no more than one merger with a mass ratio above 1:30, and the few with more mergers (up to 4 above a merger mass ratio above 1:30) do not seem to be different from the rest of the galaxy sample. Even though mergers are not the only mechanism for disc flaring, they play a key role in our sample. We do observe that if the merger is massive enough, or the mass ratio between the merger and the main galaxy is high enough, they can produce a flared thick disc, a flat age gradient, and a bimodal thin/thick disc structure. On the other hand, we observe that galaxies with a flat thick disc have a relatively quiescent merger history.
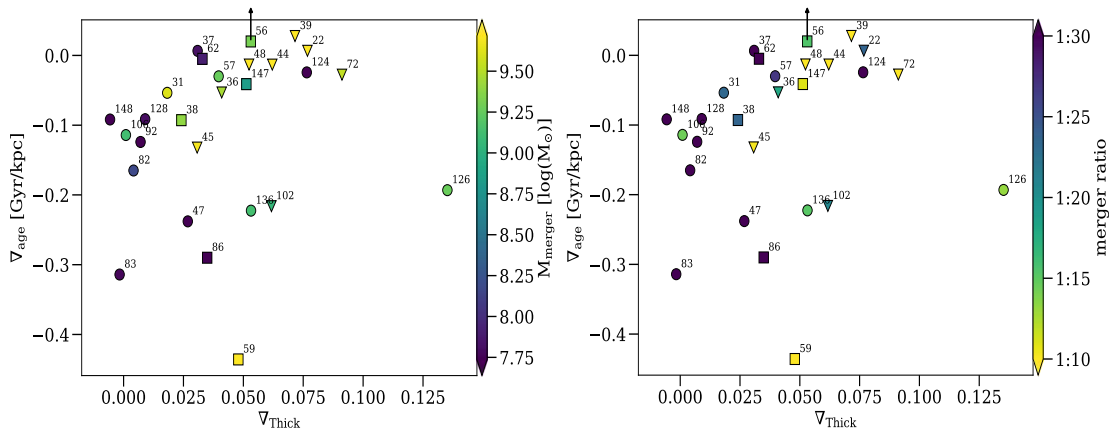

Figure 3. Age gradient following the thick disc's scale-height against the slope of the thick disc. Top: colour-coded by the mass of the most massive merger in the last 9 Gyr. Bottom: colour-coded by the mass ratio of the most massive merger in the last 9 Gyr (defined as the ratio between the stellar mass of the satellite and the main galaxy at the time of the merger) triangles represent a bimodal thin/thick structure, circles represent a continuum structure, and squares represent an intermediate case between continuum and bimodality. Galaxies with stronger mergers tend to have more flared thick discs with flatter age gradients.

4. Conclusions

In this work we explored the structure of galactic thick discs using a sample of 27 simulated galaxies in their cosmological context (Martig et al. 2012). Minchev et al. (2015) explained how Mono-Age Populations (MAPs) create the thin and thick disc by a combination of three factors: the MAPs' level of flaring, the individual MAPs' surface density, and how these two change with radius. This inter-play creates age radial gradients in the thick disc (as observed in the Milky Way, Martig et al. 2016). We expand on the work of Minchev et al. (2015) and use a sample of 27 simulated galaxies to explore: i) how the flaring of MAPs and the flaring of the global thick disc are connected, ii) whether the thin and thick discs are distinct com-ponents or a continuum, iii) what kinds of age gradients flaring MAPs form, iv) and how merger histories can potentially influence all the above. Our conclusions from this study can be summarised as follows:

• Flat thick discs form when MAPs barely flare or when, due to inside-out formation, the flared MAPs do not carry a lot of sur-face density at the flaring radii compared to younger, less flared MAPs. The MAPs' scale-heights increase smoothly as a function of age, creating a continuous thin/thick disc structure as was found for the Milky Way (Bovy et al. 2012b), although mono-age and mono-abundance populations can be quite different (Minchev et al. 2016). We find that all flat thick discs exhibit a radial age gradient like the Milky Way (Martig et al. 2016), and they are galaxies with low mass (e.g. $\leq 5 \times 10^{10}\ M_\odot$), thinner global discs (e.g. $\leq$1kpc), and lower thick disc mass

ratios (e.g. ≤40%). They also tend to have more quiescent merger histories, with low mass or low mass ratio mergers, or mergers only at early times. In our sample, 12 galaxies have flat thick discs, which corresponds to 44% percent of the sample.

- Flared thick discs form when MAPs carry a significant amount of surface density where they flare. The flaring of the global thick disc can be driven by a sequence of different MAPs at different radii, or only MAPs spanning a couple of Gyrs if those MAPs dominate the surface density throughout the disc, or they all share the same scale-heights. If one of the two last cases happens, then a bimodal structure is created and thin and thick disc are distinct components in terms of the stellar populations inhabiting them. This effect is directly related with the merger history as Martig et al. (2014b) pointed out using the same galaxy sample. Flared thick discs are more diverse than their flat counterparts in terms of age radial profiles, although a high fraction of them show a small or flat age radial profile following their thick disc's scale-heights. This is especially the case for galaxies with high mass, high thick disc mass fractions, and the thickest global discs. We also find that galaxies that underwent very massive mergers or with high mass merger ratio tend to have flat age radial profiles. In our sample, 15 galaxies have flared thick discs, which corresponds to 56% percent of the sample

Our sample of simulated galaxies thus shows a great diversity of thick disc structures, even though we only studied a relatively limited halo mass range and restricted ourselves to galaxies in isolated environments. We find a group of 6 galaxies that show characteristics close to the Milky Way, like radial age gradients in their thick discs, and minimal flaring of the global thick discs' scale-heights. These galaxies belong to the lower end of the distribution in our sample in terms of stellar mass ($\leq 5 \times 10^{10}$ $M_{\odot}$), have average thick disc scale-heights (≤1kpc), and are in the lower half of the distribution in terms of thick disc stellar mass ratio (≤40%). The rest of the sample, i.e. flared thick disc galaxies, is a lot more diverse, depending on the galaxies' formation histories. Our results cannot be directly compared to galaxies in the Fornax cluster (Pinna et al. 2019a,b), but they could be used to interpret, for instance, the discovery in NGC 7572 of a very massive and flared thick disc (Kasparova et al. 2020): this probably results from a massive merger. Our simulations suggest that thick discs can be successfully used to probe galaxies' merger histories, which we will study in more details in future papers. As more and more data become available for thick discs in nearby galaxies, we will soon be able to compare the Milky Way and its neighbours, to interpret their different structures, and to connect those with their formation histories.

References
Agertz O., Renaud F., Andersson E. P., Read J. I., Ryde N., Bensby T., Rey M. P., Feuillet D. K., 2020, Monthly Notices of the Royal Astronomical Society, 000, 0
Amôres E. B., Robin A. C., Reylé C., 2017, Astronomy and Astrophysics,602, 67
Bennett M., Bovy J., 2019, MNRAS, 482, 1417
Bournaud F., Combes F., 2002, Astronomy and Astrophysics, 392, 83
Bournaud F., Combes F., 2003, Astronomy and Astrophysics, 401, 817
Bournaud F., Elmegreen B. G., Martig M., 2009, Astrophysical Journal,707, L1
Bovy J., Rix H. W., Hogg D. W., 2012a, Astrophysical Journal, 751, 131
Bovy J., Rix H. W., Liu C., Hogg D. W., Beers T. C., Lee Y. S., 2012b, Astrophysical Journal, 753, 148
Buck T., 2020, Monthly Notices of the Royal Astronomical Society, 491,5435
Burstein D., 1979, The Astrophysical Journal, 234, 829
Comerón S., et al., 2011, Astrophysical Journal, 741, 28
Comerón S., et al., 2012, Astrophysical Journal, 759, 98
Comerón S., Elmegreen B. G., Salo H., Laurikainen E., Holwerda B. W.,Knapen J. H., 2014, Astronomy and Astrophysics, 571, 58
Comerón S., Salo H., Janz J., Laurikainen E., Yoachim P., 2015, A&A, 584,34
Comerón S., Salo H., Peletier R. F., Mentz J., 2016, A&A, 593, 6
Comerón S., Salo H., Knapen J. H., 2018, Astronomy and Astrophysics,610, 5
Dalcanton J. J., Bernstein R. A., 2002, The Astronomical Journal, 124, 1328
Feuillet D. K., Frankel N., Lind K., Frinchaboy P. M., García-HernándezD. A., Lane R. R., Nitschelm C., Roman-Lopes A., 2019, Monthly Notices of the Royal Astronomical Society, 489, 1742
Foreman-Mackey D., Hogg D. W., Lang D., Goodman J., 2013, Publications of the Astronomical Society of the Pacific, 125, 306
Gilmore G., Reid N., 1983, Monthly Notices of the Royal AstronomicalSociety, 202, 1025
Grand R. J., Kawata D., Cropper M., 2014, Monthly Notices of the RoyalAstronomical Society, 439, 623
Grand R. J. J., Springel V., Gómez F. A., Marinacci F., Pakmor R., CampbellD. J. R., Jenkins A., 2016, MNRAS, 459, 199

Jungwiert B., Combes F., Palous J., 2001, Astronomy and Astrophysics,376, 85

Jurić M., et al., 2008, The Astrophysical Journal, 673, 864

Kalberla P. M., Kerp J., Dedes L., Haud U., 2014, Astrophysical Journal,794, 90

Kasparova A. V., Katkov I. Y., Chilingarian I. V., Silchenko O. K., MoiseevA. V., Borisov S. B., 2016, Monthly Notices of the Royal Astronomical Society: Letters, 460, L89

Kasparova A. V., Katkov I. Y., Chilingarian I. V., 2020, Monthly Notices of the Royal Astronomical Society, 493, 5464

Kazantzidis S., Bullock J. S., Zentner A. R., Kravtsov A. V., MoustakasL. A., 2008, The Astrophysical Journal, 688, 254

Kazantzidis S., Zentner A. R., Kravtsov A. V., Bullock J. S., Debattista V. P.,2009, Astrophysical Journal, 700, 1896

Kennicutt Jr. R. C., 1998, The Astrophysical Journal, 498, 541

Loebman S. R., Roškar R., Debattista V. P., Ivezic Z., Quinn T. R., WadsleyJ., 2011, Astrophysical Journal, 737

López-Corredoira M., Molgó J., 2014, Astronomy and Astrophysics, 567,106

López-Corredoira M., Prieto C. A., Garzón F., Wang H., Liu C., Deng L.,2018, Astronomy and Astrophysics, 612, L8

Ma X., Hopkins P. F., Wetzel A. R., Kirby E. N., Anglés-Alcázar D., Faucher-Giguère C. A., Kereš D., Quataert E., 2017, Monthly Notices of the Royal Astronomical Society, 467, 2490

Martig M., Bournaud F., 2010, Astrophysical Journal Letters, 714, 275

Martig M., Bournaud F., Teyssier R., Dekel A., 2009, Astrophysical Journal,707, 250

Martig M., Bournaud F., Croton D. J., Dekel A., Teyssier R., 2012, Astro-physical Journal, 756, 26

Martig M., Minchev I., Flynn C., 2014a, MNRAS, 442, 2474

Martig M., Minchev I., Flynn C., 2014b, Monthly Notices of the Royal Astronomical Society, 443, 2452

Martig M., Minchev I., Ness M., Fouesneau M., Rix H.-W., 2016, The Astrophysical Journal, 831, 139

Mateu C., Katherina Vivas A., 2018, Monthly Notices of the Royal Astronomical Society, 479, 211

Minchev I., Famaey B., Quillen A. C., Di Matteo P., Combes F., Vlajić M., Erwin P., Bland-Hawthorn J., 2012a, Astronomy and Astrophysics, 548,A126

Minchev I., Famaey B., Quillen A. C., Dehnen W., Martig M., Siebert A.,2012b, Astronomy and Astrophysics, 548, A127

Minchev I., Chiappini C., Martig M., 2014, Astronomy and Astrophysics,572, A92

Minchev I., Martig M., Streich D., Scannapieco C., De Jong R. S., SteinmetzM., 2015, Astrophysical Journal Letters, 804, L9

Minchev I., Steinmetz M., Chiappini C., Martig M., Anders F., Matijevic G., Jong R. S. d., 2016, The Astrophysical Journal, 834, 27

Minchev I., et al., 2019, Monthly Notices of the Royal Astronomical Society,487, 3946

Moetazedian R., Just A., 2016, Monthly Notices of the Royal Astronomical Society, 459, 2905

Mosenkov A., et al., 2020, Monthly Notices of the Royal Astronomical Society, 494, 1751

Mould J., 2005, The Astronomical Journal, 129, 698

Narayan C. A., Jog C. J., 2002, Origin of radially increasing stellar scale-height in a galactic disk, doi:10.1051/0004-6361:20020961,http://www.aanda.org/10.1051/0004-6361:20020961

Navarro J. F., Abadi M. G., Venn K. A., Freeman K. C., Anguiano B., 2011, Monthly Notices of the Royal Astronomical Society, 412, 1203

Navarro J. F., et al., 2018, Monthly Notices of the Royal Astronomical Society, 476, 3648

Ness M., Hogg D. W., Rix H.-W., Martig M., Pinsonneault M. H., Ho A.Y. Q., 2016, The Astrophysical Journal, 823, 114

Pinna F., et al., 2019a, Astronomy and Astrophysics, 623, A19

Pinna F., et al., 2019b, Astronomy and Astrophysics, 625, A95

Polido P., Jablonski F., Lépine J. R., 2013, Astrophysical Journal, 778, 32

Qu Y., Di Matteo P., Lehnert M. D., Van Driel W., 2011, Astronomy and Astrophysics, 530

Read J. I., Lake G., Agertz O., Debattista V. P., 2008, Monthly Notices of the Royal Astronomical Society, 389, 1041

Reylé C., Marshall D. J., Robin A. C., Schultheis M., 2009, Astronomy and Astrophysics, 495, 819

Robin A. C., Reylé C., Fliri J., Czekaj M., Robert C. P., Martins A. M.,2014a, Astronomy and Astrophysics, 569, 13

Robin A. C., Reylé C., Fliri J., Czekaj M., Robert C. P., Martins A. M.,2014b, Astronomy and Astrophysics, 569, A13

Sarkar S., Jog C. J., 2019, Astronomy & Astrophysics, 628, A58

Seth A. C., Dalcanton J. J., de Jong R. S., 2005, The Astronomical Journal,130, 1574

Teyssier R., 2002, Astronomy and Astrophysics, 385, 337

Thomas G. F., et al., 2018, Monthly Notices of the Royal Astronomical Society, 481, 5223

Tsikoudi V., 1979, The Astrophysical Journal, 234, 842

Virtanen P., et al., 2019, Technical report, SciPy 1.0-Fundamental Algorithms for Scientific Computing in Python

Xiang M., et al., 2017, The Astrophysical Journal Supplement Series, 232,2

Xiang M., et al., 2018, The Astrophysical Journal Supplement Series, 237,33

Yoachim P., Dalcanton J. J., 2006, The Astronomical Journal, 131, 226

Yoachim P., Dalcanton J. J., 2008, The Astrophysical Journal, 683, 707

Charuni Wijerathne

Postgraduate Researcher

School of Civil Engineering and Built Environment

A Novel Model to Aid Design of Electrocoagulation Water Treatment Systems: Conceptual Basis and Development

DMC Wijerathne, I Carnacina, KS Hashim, CB Harris, SK Weragoda[1]

School of Civil Engineering and Built Environment / Faculty of Engineering & Technology, Liverpool John Moores University, Byrom Street, Liverpool UK, L3 3AF

[1]China Sri Lanka Research Grant Project, National Water Supply & Drainage Board, 3/90, Pahala Kondadeniya, Katugastota, Sri Lanka,

E-mail address: c.wijerathne@2017.ljmu.ac.uk

Abstract. The rising global population and poor water management strategies constitute the increasing need for sustainable water and wastewater treatment all around the world. Among the numerous technologies in use at present, electrocoagulation (EC) is considered effective and efficient in-terms of pollutant removal and energy consumption. Unaddressed challenges of EC design and optimization have hindered the widespread use of EC for water treatment around the world. This paper presents a novel, integrated model for the design of water treatment plants utilising the EC processes. The novel process based conceptual model evaluates the key processes of the treatment system and their aggregate effect in the removal of constituents. Component process models were developed and validated in MATLAB using batch EC reactor experimental data extracted from the literature.

Nearly 2.1 billion People, lacked access to safely managed water services in 2015(WHO/UNICEF, 2017) which accounts for 29% of the global population. Water treatment systems are important to supply contaminant free, safe drinking water to society to support life and avoid potentially fatal illness. However, these treatment methods are often chemically, operationally and economically intensive. Hence, the applicability of such schemes in developing nations is limited. Considerable infusion of capital, engineering expertise and infrastructure precludes their use in most parts of the world. Sustainable, affordable, safe and robust methods to increase supplies and purify water should be developed and implemented to serve people throughout the world (Shannon et al., 2008).

Among the numerous technologies in use at present, the electrocoagulation (EC) process in water and wastewater treatment has emerged as being popular during the last two decades. Efficient pollutant removal, low energy consumption and the automation possibility are among the top reasons for increased EC related research during the recent past. The conventional statistical optimization of the EC process involves numerous test runs and results in poor optimization. The literature demonstrated a scarcity of systematic design and modelling approaches.

The science that governs and makes EC standout from the conventional treatment systems is the Electrochemistry. Electrochemistry is a complex science accompanied by charge transport, electrochemical kinetics, knowledge of electrode interface and thermodynamics. Hence, studying mass and energy transfer under the effect of electrochemistry in EC is an utmost necessity to fully benefit from the technology.

The general processes associated with conventional water treatment systems (coagulation, flocculation, settling or flotation) occur simultaneously inside the EC reactor. Figure 1 illustrates the interdependent nature of the EC process.
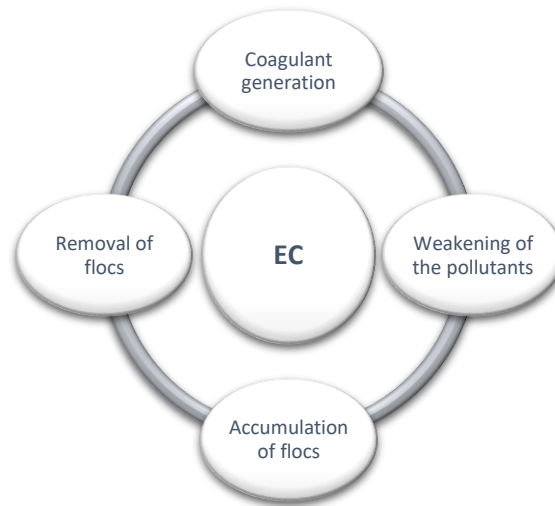
Figure 1: Interactions occurring within an EC reactor

Presented in this paper is the development of a novel, integrated model of the EC process kinetics applicable to drinking water treatment. This model is distinct from previous efforts in the literature (e.g. Emamjomeh, 2011; Sulaymon, 2012; Dubrawski et al., 2014; Andreas, 2014). The model developed here emphasises a conceptual, rather than statistical, basis for each process considered and the cumulative effect thereof. The pollutant's interactions within the system and eventual removal paths are determined by the physicochemical properties of the pollutant. The modelling of EC is governed by the second process, which is the weakening of the pollutants that could occur in numerous ways. Hence, this study will focus on fluoride removal using aluminium electrodes to gain the advantage of the vast body of knowledge from related studies. The component processes included in the model are electrolysis, hydrolysis, coagulation, flocculation together with settling and flotation (figure 2).
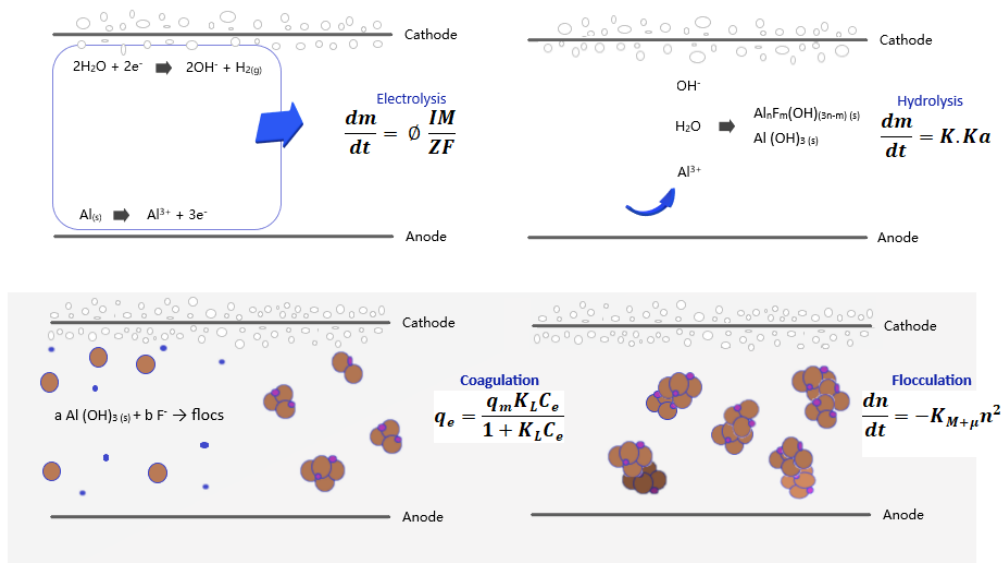
Figure 2: The component processes used for the fluoride removal model

Initial implementation of the conceptual models, and their performance against secondary data, was explored using MATLAB. This evaluated the validity of the individual component processes in both sequential and simultaneous operational configurations and assessed the known calibration protocols.
The associated calibration parameters of the process based conceptual model (PBCM) are listed below.

ε; the correction factor, denoted Al(OH)3 outflow from previous time gap
qm; the maximum adsorption capacity (mg g−1)
KL; the Langmuir constant (L/mol)

K; a percentage denoted hydrolysis efficiency
dj; colloid size which participate in adsorption process (m)
di; colloid size which participate in flocculation process (m)
G; the velocity gradient in the orthokinetic model used in flocculation (s-1)
α; the correction factor, denoted adsorption of dissolved fluoride on electrodes

The results of root means square error (RMSE) between the PBCM and the Emamjomeh (2006) data was studied against the calibration parameters using a trial and error method. The approach yielded promising results, with a lowest RMSE of 0.3586 reported for the experiment with data collected for a supply current of 1.5A using a batch reactor reported by Emamjomeh (2006) (figure 3).
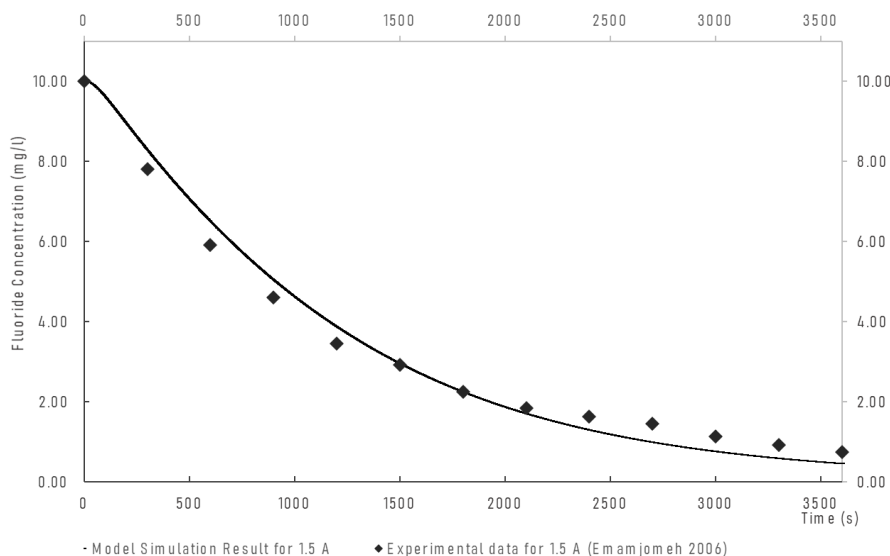
Figure 1.3: The model simulations for fluoride removal & Emamjomeh 2006 data for I = 1.5 A

The significance of the contribution from this research is a novel PBCM that could predict the pollutant abatement process in EC reactors. Rather than using a generic simulation approach, this model will be able to evaluate the significance of each process, hence allowing the designers to have more control over the process variables. This could significantly impact EC water treatment process designs by providing designers with the ability to optimize and scale-up the treatment process economically.

Acknowledgments

References

Andreas, O. 2014 *The Dim-DoE framework for Scale-Up in Chemical Engineering.* Technical Report, Umesoft GmbH**, Eschborn, Germany**

Dubrawski, K. L. & Mohseni, M. 2013 In-situ identification of iron electrocoagulation speciation and application for natural organic matter (NOM) removal. *Water Research,* **47,** 5371-5380.

Emamjomeh, M. M., *Electrocoagulation technology as a process for defluoridation in water treatment*, Doctor of Philosophy thesis, School of Civil, Mining and Environmental Engineering, University of Wollongong, 2006. http.//ro.uow.edu.au/theses/1923

Emamjomeh, M. M., Sivakumar, M. & Varyani, A. S. 2011. Analysis and the understanding of fluoride removal mechanisms by an electrocoagulation/flotation (ECF) process. *Desalination*, 275, 102-106.

Shannon, M. A., Bohn, P. W., Elimelech, M., Georgiadis, J. G., Mariñas, B. J. & Mayes, A. M. 2008. Science and technology for water purification in the coming decades. *Nature*, 452, 301.

Sulaymon, A. H. and Abbar, A. H. 2012 Scale-Up of Electrochemical Reactors. In *Electrolysis*; Kleperis, J., Ed.; InTech: Rijeka, Croatia. Available from https://www.intechopen.com/books/electrolysis/scale-up-of-electrochemical-reactors

WHO/UNICEF 2017. *Progress on Drinking Water, Sanitation and Hygiene*: 2017 Update and SDG Baselines. Geneva: WHO/UNICEF

Kingsley Madubuike

Postgraduate Researcher

School of Engineering

Fault diagnosis and fault tolerant control of a variable speed pitch angle hydraulic system

K Madubuike*, C Mayhew*, Q Zhang*, B Gomm* and Ding-Li Yu*

* Control System Research Group, Liverpool John Moores University, Liverpool, UK.

Abstract

To improve the reliability of the wind turbine system., a variable speed wind turbine pitch angle control which can tolerate and detect faults is designed. The pitch angle system consists consists of a hydraulic motor, Pitch gear set, two relief valves and a variable speed hydraulic pump. The fault diagnosed here is the shaft rotary friction change which is caused by the break of shift or pitch gear set. The proposed fault tolerant control (FTC) method uses a disturbance observer to diagnose the fault. The FTC is implemented using the combination of a neural network (NN) estimator and a full order terminal sliding mode control. The post fault states can drive to the sliding surface and converge in finite time. The control law is derived using a lyapunov stability method to ensure we guarantee stability for post-fault. A third order nonlinear state space is derived, and physical parameters applied in the simulation. The simulation results are presented to validate the effectiveness of the proposed scheme. Matlab and Simulink is used to simulate the electrohydraulic servo pitch system with the faults simulated.

Keywords: fault detection, fault tolerant control, hydraulic pitch system.

1.Introduction

Fault detection and fault tolerant control has been effective in enhancing the reliability of complex control systems in modern industry [2]. The job of fault detection is to report fault occurrences within a control system and to stabilize the post fault dynamics [2]. Terminal sliding mode control is very effective in making nonlinear systems to achieve finite time convergence and robustness to system uncertainties [4]. The two main problems encountered when using TSM is its singularity and chattering. The chattering problem is because of the discontinuous terms present in the control that leads to high frequency oscillation across the TSM. The existence of negative fractional powers in the control causes singularity. It has the tendency of damaging the actuator device. These characteristics are undesirable in practices. A novel method was proposed recently in [1]. Here the TSM designed is of full order. This means that the TSM and system model has the same states. The full order terminal sliding mode (FOTSM) has some characteristics like avoidance of singularity and chattering. The FOTSM proposed here needs previous knowledge of the bounds of derivatives which are difficult to get in practice. This limitation has imparted the acceptance of this method in practice.

In this paper, we investigate application of FOTSM combined with a disturbance observer to achieve fault detection and fault tolerant control of a variable speed hydraulic pitch system. The change rate of the fault is estimated using a radial basis function (RBF) neural network. This new method must be able to tolerate the fault without previous knowledge of the bounds of derivatives. The fault which is the nonlinear dynamics of the viscous and coulomb frictions of the hydraulic motor has a major change in practice to obstruct normal operation of the system. The rest of the paper are structured as follows; the hydraulic pump and the faut were modelled. The next section details the design of the disturbance observer for fault detection. The next section outlines the fault tolerant control scheme including the lyapunov stability and the simulation results will be discussed in the next section. Matlab and Simulink will be used to simulate the fault and discuss.

2. Hydraulic system modelling

The pitch angle system proposed in this research consists of a hydraulic motor, Pitch gear set two relief valves and a variable speed hydraulic pump. The schematic diagram of the hydraulic pitch drive system can be found in figure 1.
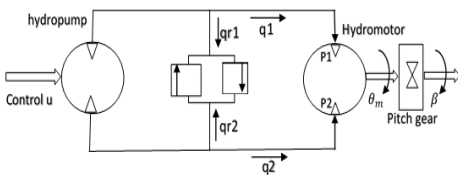

Figure 1: Schematic of pitch angle drive system

The pitch angle system dynamics is presented in (1.01) [3]

$$\ddot{\theta} = \frac{1}{j_t}[D_m(\dot{P}_1 - \dot{P}_2) - G\ddot{\theta}_m - \dot{T}_p] \qquad (1.01)$$

41

A 3rd order state space model is set up using (1.01) by defining the state variables as $x_1 = \beta(t), x_2 = \dot{\beta}, x_3 = \ddot{\beta}$.

$$\dot{x}_1 = x_2$$
$$\dot{x}_2 = x_3$$
$$\dot{x}_3 = \frac{D_m \beta_e}{J_t(v_1 + D_m i_g x_1)}\left[-D_m x_2 - \frac{(C_{tp}+C_{tm})}{D_m}\left(J_t x_3 + G x_1 + \frac{T_p(t)}{i_g}\right) + \frac{D_p K_a}{i_g}u(t)\right] - \frac{D_m \beta_e}{J_t(v_2 - D_m i_g x_1)}\left[-D_p x_2 + \frac{(C_{tp}-C_{tm})}{D_m}\left(J_t x_3 + G x_1 + \frac{T_p(t)}{i_g}\right) - \frac{D_p K_a}{i_g}u(t)\right] - \frac{G}{J_t}x_3 - \frac{\dot{T}_p}{J_t i_g} \qquad (1.02)$$

Where the leakage coefficient of the hydraulic pump and motor are denoted as C_{tp} and C_{tm} respectively. The general form of (1.02) is formulated as follows

$$\dot{x}_3 = g(x) + b(x)u(t) + f(t) \qquad (1.03)$$

Where

$$g(x) = -\frac{D_m \beta_e}{J_t}\left\{\frac{1}{v_1 + D_m i_g x_1}\left[D_m x_2 \frac{C_{tp} + C_{tm}}{D_m}(J_t x_3 + G x_1)\right] + \frac{1}{v_2 - D_m i_g x_1}\left[D_m x_2 + \frac{C_{tp} + C_{tm}}{D_m}(J_t x_3 + G x_1)\right]\right\} - \frac{G}{J_t}x_3$$

$$b(x) = \frac{D_m \beta_e D_p K_a}{J_t i_g}\left(\frac{1}{v_1 + D_m i_g x_1} + \frac{1}{v_2 - D_m i_g x_2}\right)$$

$$f(t) = -\frac{\beta_e(C_{tp} + C_{tm})}{J_t i_g} \times \frac{1}{v_1 + D_m i_g x_1} \times T_p(t) - \frac{1}{J_t i_g}\dot{T}_p(t)$$

Where $f(t)$ represents the fault signal to be detected and tolerated in the control system designed. In this thesis $f(t)$ is a function of $T_p(t)$ and derivative of $\dot{T}_p(t)$. $T_p(t)$ is the added viscous and column friction of pitch system axis and gear set. This is caused by a frequently occurred system(component) failure in a wind turbine system. The physical parameters in the model are listed below;

$K_a=0.5, D_p = 0.03, C_{tp} = 0.5*10^{-11,} \beta_e = 2.0 * 10^{-9}, V_1 = 0.01, V_2 = 0.04, D_m = 0.002.[2]$

3. Disturbance observer

A disturbance observer (DO) is designed to detect fault in the variable speed pitch angle system. A model following vector-matrix form is presented for system models (1.03).

$$\dot{x}_1 = f(x) + g_1(x)u(t) + g_2 d(t) \qquad (1.04)$$

Where $x = [0\ 0\ b(x)]$, $g_2 = [0\ 0\ 1]^T$. x is the system state. $u \in R$ is system input, $g(x)$ and $b(x)$ are smooth nonlinear function with $g(0) = 0$ and $b(x) \neq 0$. $d(t)$ is the system fault. It is assumed that $\dot{d}(t)$ is bounded and continuous and the knowledge of the bounds is not needed. This assumption is generally satisfied in engineering problems.

A disturbance observer for (1.04) is designed in (1.05)

$$\begin{cases} \dot{z} = -P g_2 z - P[g_2 P + f(x) + g_1(x) \\ \hat{f} = z + Px \end{cases} \qquad (1.05)$$

where $z \in R$, $P \in R^{1 \times 3}$ and $\hat{f}$ are the internal state variable, observer gain matrix and output of the observer or the fault estimate respectively. The fault estimation error will converge to zero if the fault is a constant signal.

4. Fault tolerant control scheme

For the fault tolerant control scheme, a robust full order terminal sliding mode control scheme is designed with an RBF network updated online to compensate the effects of the faults. A disturbance observer is developed to help in fault detection and for fault tolerant control. The control system for the nonlinear hydraulic pitch system is designed in a way that the output x_1 tracks the refrence signal such that when a fault occurs, the stability of the closed loop system is guaranteed with the fault not influencing the tracking performance. The use of FOTSM control technique makes the system states reach the TSM and then converge to the equilibrium in finite time. The chattering phenomenon is eliminated because the controller uses the forms of integrator or low pass filter. For an nth order nonlinear system as described in (1.06), a model based FOTSM control model that uses the RBF to approximate the nonlinear function was developed.

$$\begin{cases} \dot{x}_1 = x_2 \\ \dot{x}_2 = x_3 \\ \dots \\ \dot{x}_n = f(x) + d(x) + b(x)u \end{cases} \qquad (1.06)$$

Where $x = [x_1, x_2, \ldots, x_n]^T \in R^n$ is the system state $u \in R$ is the system input, $f(x)$ and $b(x)$ denotes Continuous nonlinear functions with $f(0) = 0$ and $b(x) \neq 0$. The fault signal of the system is denoted as $d(x)$. There is an assumption that the first order derivative of the fault $\dot{d}(x)$ is bounded and a continuous function. The bound of the fault change in the system is unknown.

A FOTSM manifold definition used here when compared to the definition in [1] looks similar. The difference is that the tracking error is used for the reference tracking control instead of the system state.

$$s = \dot{e}_n + \beta_n e_n^{a^n} + \ldots \beta_1 e_1^{a^1} \qquad (1.07)$$

Where e_i $(i = 1, 2, \ldots, n)$ as defined below is the tracking error with $r(t)$ being the reference output.

$$\begin{cases} e_1 = x_1 - r \\ e_2 = \dot{e}_1 = \dot{x}_1 - \dot{r} \\ \quad \ldots \\ e_n = \dot{e}_{n-1} \end{cases} \qquad (1.08)$$

When β_i $(i = 1, 2, \ldots, n)$ is designed the condition that the polynomial $p^n + \beta_n p^{n-1} + \cdots + \beta_2 p^1 + \beta_1$ is Hurwitz is fulfilled. $\alpha_i (i = 1, 2, \ldots, n)$ is designed as

$$\begin{cases} a_1 = a_2 & n = 1 \\ a_{i-1} = \frac{a_i a_{(i+1)}}{2a_{i+1} - a_i} & i = 2, \ldots, n \ \forall n \geq 2 \end{cases} \qquad (1.09)$$

Where $a_{n+1} = 1$, $a_n = a$, $a \in (1 - \varepsilon, 1)$, $\epsilon \in (0,1)$. Once a FOTSM is achieved s=0 is reached and the tracking error in (1.08) will converge to zero and converge to the terminal sliding mode within finite time. A new method is developed to guarantee finite time convergence of the tracking error and system states without knowledge of fault and fault derivatives. The RBF estimator will be used to approximate the fault derivative. This new method combines the online estimation of the fault change rate by an adaptive RBF network and a model FOTSM to drive the states onto the sliding surface. The Rbf network is used to estimate the fault derivative $\dot{d}(x)$ from the current system state and it is defined as (1.10).

$$\dot{d}(x) = W^T \emptyset(y) + \epsilon \qquad (1.10)$$

Where the approximation error is denoted as , $y = [x_1, \ldots, x_n, \dot{x}_n]$ is the Rbf input vector. The nonlinear basis function is presented as
$\emptyset(y) = [\emptyset_1(y), \emptyset_2(y), \ldots, \emptyset_i(y)]^T \in R^l$, $W = [w_1, w_2, \ldots, w_i]^T \in R^l$ is the weight vector. The Gaussian function can be expressed in (1.11)

$$\emptyset(y) = \exp\left(-\frac{||y - c_i||^2}{\omega_i^2}\right) i = 1, \ldots, l \qquad (1.11)$$

Where c_i is the centre of the ith hidden layer node. w_i is the radius of the ith Gaussian function. The controller is designed below based on the Rbf neural network and the FOTSM manifold in (1.07)

$$u = b^{-1}(x)(u_1 + u_2) \qquad (1.12)$$

$$u_1 = -g(x) - \beta_n e_n^{a_n} - \ldots - \beta_1 e_1^{a_1} + \ddot{r} \qquad (1.13)$$

$$\dot{u}_2 = -W^T \emptyset(y) - (k + \eta) sgn(s) \qquad (1.14)$$

Where $K > \epsilon_N$, $\eta > 0$, the signum function is denoted as sgn (0). Using the information provided by the states in the network input vector $z(x)$, the Rbf estimator is adapted online. The adaptation law is designed in (1.15)

$$\hat{W} = \frac{1}{\gamma} s\emptyset(y) \qquad (1.15)$$

Where $\gamma > 0$ is the inverse of a learning rate..

In (1.06), If the Fotsm manifold is chosen as (1.07) and the control law and network adaptation law are designed as in (1.12) – (1.15) then the state of the closed loop system will converge to zero which makes the system stable. k and η are constants to be selected for the design. For $\dot{V} < 0$, k and η are chosen such that $\eta > 0$, $k > \epsilon_N \geq \epsilon$, then $(e - k - \eta)|s| < 0$ for $s \neq 0$. The Rbf estimator weights converge to the existing optimal weights. (1.14) adopts the form of an integrator. The sign function was used in $\dot{u}_2$ instead of the u_2 to ensure that the discontinuity caused by the sign function will not directly affect the control law but will be integrated. The control signal will be guaranteed continuous. The chattering problem is eliminated due to this technique. The derivative of s is unused causing the designed control to avoid singularity. The information generated in fault detection are used to assist for fault tolerant control.

Mohsin Amin

Postgraduate Researcher

School of Civil Engineering and Built Environment

The Pathogenesis of Periodontal Disease

Amin M[a,d], Whitehead K A[a,b], Shalamanova L[b], Taylor R L[b], Wylie S[c] and Abdullah B M[d]
[a] Microbiology at Interfaces, Manchester Metropolitan University, UK
[b] Department of Life Sciences, Manchester Metropolitan University, UK
[c] Liverpool John Moores University, Department of Engineering and Technology, Civil Engineering, UK
[d] Liverpool John Moores University, Department of Engineering and Technology, Built Environment, UK

Abstract. The importance of oral health and its influence on systemic disease has been emphasised throughout history. Periodontal disease, one of the major diseases in human adult populations maintains very high affliction rates per capita. The oral cavity plays a major role in maintaining life and due to its unique design, is exposed to continual external factors. Periodontal disease presents as one of the commonest oral diseases in the human population. Initiating as gingivitis, a treatable inflammatory infection progresses to the incurable periodontitis, resulting in eventual tooth loss.

Key words: Oral disease, Periodontitis, Gingivitis, Dental biofilms

1. The Oral Cavity

The oral cavity is composed of hard and soft tissues which are continually exposed and challenged by numerous external pressures (Taylor and Preshaw, 2016). The primary structures of the oral cavity are the teeth, which enable the grinding and chewing of food to allow for ingestion, the tongue which compresses food against the palate to form bolus, and the palate, which forms a mechanical barrier to sperate the oral cavity and nasal respiratory tract (German and Palmer, 2006). The hard tissues of the oral cavity encompass the dentine, cementum and enamel which are juxtaposed against the soft tissues of the buccal mucosa, soft and hard palate, the tongue and the periodontium. The periodontium describes the tooth supporting and investing tissues such as the gingiva, root cementum, periodontal ligament, and alveolar bone (Cho and Garant, 2000).

2. Periodontal Diseases

Periodontal diseases are the most frequent oral disease of the human population. It is a microbial driven inflammatory disease caused by bacterial dental plaque (Hajishengallis, 2015). It manifests persistent inflammation of the gingiva, gingiva bleeding and the formation of the hallmarked periodontal pockets (Shatzle et al., 2004). It is estimated that between 20% – 50% of the global adult population are afflicted with periodontitis, making it the sixth most prevalent disease worldwide (Nazir, 2017). The categorisation of periodontal disease can be broken down into four stages: gingivitis, mild periodontal disease, moderate periodontal disease, and advanced periodontal disease.

3. Gingivitis

Gingivitis is a form of gingival inflammation and represents reversible inflammation, with rates as high as 90% amongst children aged 7-14 years (Ellis et al., 2007). The onset of gingivitis is suggested to be mediated by the presence of periopathogenic microorganisms of the dental plaque and its releasates (Murakami et al., 2018).

Gingivitis is solely limited to the soft tissues of the gingival epithelium and connective tissues. However, periodontitis, a more advanced form of gingivitis, presents similarly as an inflammatory infection of the supporting structures but progresses to attachment loss and bone destruction. Both inflammatory diseases are very common ailments in human populations and in both instances the disease is associated with the accumulation of bacteria at the dento-gingival margin (Saini et al., 2011).

4. Periodontitis

Periodontitis results in eventual loss of the periodontal ligament and subsequent destruction of alveolar bone by compromising the integrity of supporting tooth structures (de Pablo et al., 2009; Al Moharib et al., 2014). From initiation, the disease progresses with the detachment of collagen fibres from the root cementum, apical migration of the junctional epithelium, deepened pocket formation and finally, resorption of the alveolar bone (Tsuchida et al., 2017). Periodontitis will ultimately progress to bone destruction if untreated, leading to increased tooth mobility with subsequent tooth loss (Hienz et al., 2015).

5. Dental Biofilm Formation

The dental biofilm is comprised primarily of microorganisms which exist within an extracellular matrix, derived from the constituents of saliva, gingival crevicular fluid and bacterial products. The key characteristic of a dental biofilm is that the attachment of micro colonies present in the film to a solid surface (Frédéric et al., 2018). This successful attachment is the initial stage of dental biofilm development.

Biofilm formation occurs in multiple stages, initialising with the formation of an acquired film through the adsorption of host and bacterial molecules onto the surface of the teeth. The development of this film allows for the microorganisms which arrive at this site through active transport to interact with the film *via* Van der Waals and electrostatic forces (Bos et al., 1999). Later in the biofilm's development, the weak bond formed prior is reinforced through bacterial adhesins with the complementary receptors in the dental biofilm itself. Over time, this process of aggregation will allow for the recruitment of new colonisers and cement the formation of a biofilm (Martinez and Figuero, 2006).

6. Periodontal Lesion Formation

The initial inflammation of the periodontal tissues can be considered a physiological defence against the onset of a microbial attack. In gingivitis the clinical findings at the early stage of the disease are primarily the development of supra and sub gingival plaque, which is consequentially accompanied by the formation of calculus and gingival inflammation. Upon removal of the dental biofilm, the normal homeostasis of the oral environment resumes. However, if allowed to progress unhindered, the initial lesion is able to progress into the early, established and eventually the advanced lesion.

The initial lesion occurs in response to the activation of resident leukocytes and endothelial cells in response to the bacterial biofilm (Rathee and Jain, 2021). At this clinical stage, inflammation is still non apparent, but histological changes to the gingival tissues can be observed. In the early lesions, the increased number of neutrophils enable the activation of various complement pathways. The epithelium eventually proliferates and extends and forms rete pegs, a clinical histological observation of gingival inflammation, alongside gingival bleeding and increased gingival crevicular fluid flow (Steinfort et al., 2019). The established lesion subsequently develops within a period of 2-3 weeks after the early lesion (Page and Schroeder, 1976). The endpoint of the established lesion is the formation of the gingival pocket, due to the migration of polymorphoneuclear leukocytes through the junctional epithelium. The advanced lesion, also known as the destructive phase, is the stage at which the transition from gingivitis to periodontitis occurs.

7. Conclusion

Oral disease is represented throughout the population and demonstrates a global health concern. The oral cavity is a host to numerous foreign and host specific substances, of which bacteria are demonstrated as the key components of specific oral disease. Both gingivitis and periodontitis are bacterially mediated diseases and whilst gingivitis is curable, periodontitis remains incurable. The progress of gingivitis to periodontitis can be observed through the assessments of periodontal lesions and act as a foci for dental biofilm infiltration.

References

AlMoharib, H. S., AlMubarak, A., AlRowis, R., Geevarghese, A., Preethanath, R. S., Anil., S., 2014. Oral fluid based biomarkers in periodontal disease: part 1. Saliva. *J Int Oral Health*. 6(4), 95-103.

Bascones Martínez, A. and Figuero Ruiz, E., 2005. Periodontal diseases as bacterial infection. *Avances en Periodoncia e Implantología Oral*, 17(3).

Bos, R., van der Mei, H.C. and Busscher, H.J. (1999). Physico-chemistry of initial microbial adhesive interactions – its mechanisms and methods for study. *FEMS Microbiology Reviews*, 23(2), pp.179–230.

Cho, M. I., Garant, P. R., 2000. Development and general structure of the periodontium. *Periodontol 2000*. 24, 9-27.

de Pablo, P., Chapple, I. L., Buckley, C. D., Dietrich, T., 2009. Periodontitis in systemic rheumatic diseases. *Nat Rev Rheumatol*. 5(4), 218-224.

Ellis, S.D., Tucci, M.A., Serio, F.G. and Johnson, R.B. (2007). Factors for progression of periodontal diseases. *Journal of Oral Pathology & Medicine*, 27(3), pp.101–105.

Frédéric, L., Michel, B. and Selena, T. (2018). Oral Microbes, Biofilms and Their Role in Periodontal and Peri-Implant Diseases. *Materials*, 11(10), p.1802.

German, R. Z and Palmer, J. B. 2006. Anatomy and development of oral cavity and pharynx. GI Mot. On.

Hajishengallis, G., 2015. Periodontitis: from microbial immune subversion to systemic inflammation. *Nat Rev Immuno*. 15(1), 30-44.

Hienz, S. A., Paliwal, S., Ivanovski, S., 2015. Mechanisms of bone resorption in periodontitis. *J of Immu Res*. 615486.

Murakami, S., Mealey, B.L., Mariotti, A. and Chapple, I.L.C. (2018). Dental plaque-induced gingival conditions. *Journal of Periodontology*, 89, S17–S27.

Nazir, M. A., 2017. Prevalence of periodontal disease, its association with systemic diseases and prevention. *Int J Health Sci*. 11(2), 72-80.

Page RC, Schroeder HE. Pathogenesis of inflammatory periodontal disease. A summary of current work. Lab Invest. 1976 Mar;34(3):235-49. PMID: 765622.

Rathee, M. and Jain, P. (2021). *Gingivitis*. [Online]. Available at: https://www.ncbi.nlm.nih.gov/books/NBK557422/#:~:text=Initial%20lesion%3A%20It%20is%20the. [Accessed: 26th April 2021]

Saini, R., Saini, S. and Sharma, S., 2011. Biofilm: A dental microbial infection. *Journal of Natural Science, Biology and Medicine*, 2(1), p.71.

Schatzle, M., Loe, H., Lang, N., Burgin, W., Anerud, A., Boysen, H., 2004. The clinical course of chronic periodontitis. *J Clin Perio*. 31(12), 1122-1127.

Steinfort, S., Röcken, M., Vogelsberg, J., Failing, K. and Staszyk, C. (2019). The Equine Gingiva: A Histological Evaluation. *Frontiers in Veterinary Science*, 6.

Taylor, J. J., Preshaw, P. M., 2016. Gingival crevicular fluid and saliva. *Periodontol 2000*. 70(1), 7-10.

Tsuchida, S., Satoh, M., Takiwaki, M., Nomura, F., 2017. Ubiquitination in periodontal disease: a review. *Int J Mol Sci*. 18(7), 28698506.

Kang Ji

Postgraduate Researcher

School of Engineering

A Virtual Force-based Strategy for Multi-robot Deployment

Kang Ji, Qian Zhang, Dingli Yu

School of Engineering, Liverpool John Moores University, Liverpool, 3 Byrom Street, Liverpool, L3 3AF, UK

K.ji@2017.ljmu.ac.uk, Q.Zhang@ljmu.ac.uk, D.Yu@ljmu.ac.uk

Abstract. In this paper, a task of autonomous robots' deployment for satisfying the requirements of targets (landmarks) in the specific scenes is tackled, where it aims to reach a final deployment of agents with full target coverage. A virtual force-based distributed coordination strategy among agents and the environment is proposed to accomplish the task. In this algorithm, each agent consecutively updates its position according to the varying virtual forces it bears, and the final target coverage deployment is obtained after several iterations. The designed approach has been assessed in a series of simulation experiments with different configurations. The simulation results demonstrate the effectiveness of the proposed approach. The main contribution of this paper is to modify the virtual force algorithm to account for target coverage.

1. Introduction

In the last decade, application of autonomous mobile robots has gained growing attention. Compared with a single robot, a multi-robot system is more suitable and advantageous for applications such as environmental monitoring, battlefield surveillance, and search and rescue. It seems more advantageous and attractive in multi-robot cooperative work over a single-robot approach for such complex tasks. The autonomous deployment of a group of robotic agents with certain sensing capabilities for satisfying the need of landmark targets in the specific scene is tackled in this paper. When agents perform exploration and search processes simultaneously, the lack of coordination may cause exploration redundancy. It is crucial to introduce a distributed coordination method to avoid overlapped exploration information for searching targets in effectiveness and efficiency. A simple local virtual force strategy relied only on the local sensing information and communication is proposed to determine the movement of each agent in the exploration process until the agent stop at its discovered target.

The virtual force algorithm (VFA) has been used widely to achieve uniform distributions of robots. The virtual force for the deployment of wireless sensor nodes was firstly proposed by Zou et al. [1]. In VFA, the attractive force and repulsive force between nodes are defined for increasing coverage. His method is not suitable for the environment with many obstacles due to only the simple repulsive force from the obstacle is defined and test in the environment with only one obstacle. Research on the improved virtual force-based method for coverage control contains introducing Delaunay triangulation to set the adjacent relationship to increase computation efficiency [2] introducing energy awareness for each agent in the virtual force method to balance their energy consumption [3] and combining the VFA with particle Swarm optimization for global search ability [4]. In [5], new vortex forces are designed to cooperate with repulsive forces to find a good balance between global exploration of the whole environment and local exploitation for better coverage considering the complex environment and the large scale of agents. Different from all the above studies, where the focus is on achieving uniform distribution of the robots and a central coordinator may be utilized, we modify the virtual force algorithm to account for the criticality of several preferential target points (landmarks) based on interaction among robots and landmarks and to ensure a fully distributed deployment.

2. Methodology for the target search problem

2.1. Problem description

In the target search problem, several unknown target landmarks in a predefined bounded environment require discovery and coverage by a group of homogeneous robotic agents simultaneously. Each agent is assumed to have no prior knowledge of targets' locations and obstacles in the 2D plane environment and have the capability of localization, sensing environment, and local communication. Each agent is able to monitor its surrounding environment and plan motions in its limited-range circular perception range   , exchange information with other agents in its communication range   which is larger than the sensing range, and detect the target's direction when the target is in the communication range. We considered that agents are initially distributed aligned to the boundary of the environment or inside environment.

2.2. Virtual Force-based Strategy

R_e

When agents perform exploration and search processes simultaneously, the lack of coordination may cause exploration redundancy. It is crucial to introduce a distributed coordination method to avoid overlapped exploration information for searching targets in effectiveness and efficiency. A simple local virtual force strategy relied only on the local sensing information and communication is proposed to determine the movement of each agent in the exploration process until the agent stop at its discovered target.

In our method, each agent can respond to its current environmental perception and communication via the virtual forces, which include the repulsive force from other nearby communicated agents, its own last two historical positions and the detected border of the defined environment, and the attractive force from the closed communicated target which would shield the repulsive force. The direction of the combined force exerted upon the agent determines each agent's next movement heading direction for updating the agents' positions iteratively. When one agent achieves communication with one target, it can be informed of the relative directional information of the target and is motivated to move heading to the communicated target, which can be formalized in an attractive force upon the agent from the target. When the agent is connected to at least one target, the attractive force $\overrightarrow{F_{ia}}$ only depends on its closest communicated target. When $\overrightarrow{F_{ia}}$ is not zero, it will shield all other virtual force calculation and reach to the target as the attractive force's direction. The repulsive force among agents enables them to spread themselves to accelerate the exploration process. The repulsive force $\overrightarrow{F_{ij}}$ is exerted upon the agent a_i from a_j when their distance is no more than a threshold. The repulsive force from its historical position enables to reduce the exploration redundancy. $\overrightarrow{F_{i,h(k)}}$ is defined as the repulsive force exerted upon the agent a_i from its last kth position. For staying away from the environment border, the repulsive force $\overrightarrow{F_{ib}}$ between the agent and the detected environment boundary is introduced. Only when the agent is initialized at the location without the above virtual force, we introduce a starting virtual force with a random direction $\overrightarrow{F_{is}}$ to stimulate the agent to leave away and start exploration in its earliest stage, otherwise, it is zero. The combined repulsive force $\overrightarrow{F_{ir}}$ on the agent a_i is calculated as (5). When the agent has not detected the target or has not arrived at the target, the next position is calculated as (6-7).

$$\overrightarrow{F_{ir}} = \sum_{j=1, j\neq i}^{N_a} \overrightarrow{F_{ij}} + \sum_{k=1}^{2} \overrightarrow{F_{i,h(k)}} + \overrightarrow{F_{ibr}} + \overrightarrow{F_{is}}$$

$$x_{i,c}(t+1) = x_i(t) + M \times sign\left(\overrightarrow{F_{ir,x}}\right)$$

$$y_{i,c}(t+1) = y_i(t) + M \times sign\left(\overrightarrow{F_{ir,y}}\right)$$

N_a is the number of agents, ($x_i(t)$ $y_i(t)$) and ($x_{i,c}(t+1)$, $y_{i,c}(t+1)$) is the current position and newly calculated position of the agent; M is the movement step size; $\overrightarrow{F_{ir,x}}$ and $\overrightarrow{F_{ir,y}}$ are the component forces of $\overrightarrow{F_{ir}}$ along the x-coordinate and y-coordinate respectively.
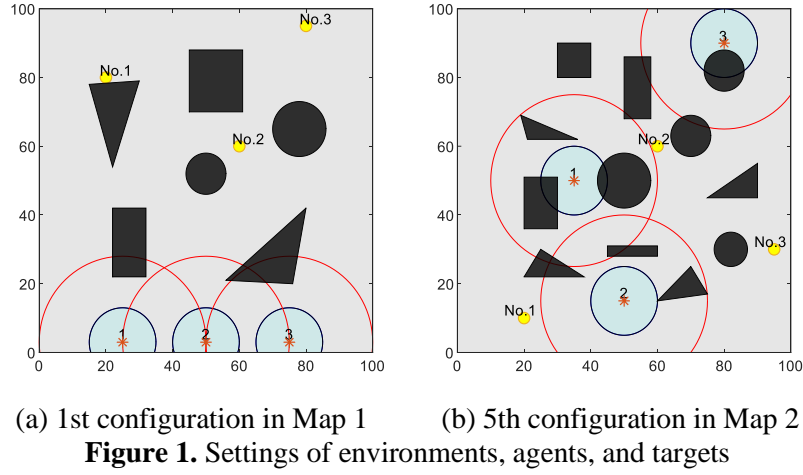
The calculated position may fall into the unmovable area, so it requires verification and potential modification. If the calculated position is in the movable free space, it moves there at the end of the iteration. If the calculated position falls into the prohibited area, the cross points of the continuous detected obstacle border and the continuous detected environment border with the perception frontier are determined firstly, and then the optional positions are selected by deflecting vector from the current position to these cross points by 10-degree angle rotation to the free space direction and taking points according to step size along these directions and finally the optional position nearest to the original calculated position in the perception area is chosen.

The process of the proposed strategy can be summarized as three key sections in each iteration before reaching the target: the calculation of virtual force, the calculation of agent position, and the movable verification and potential modification. Each agent will consecutively update positions using this strategy until it arrives at the discovered target's location.

3. Experiments and Results

3.1. Experiment environment setting

The experiments are conducted through simulation in MATLAB. The environment is expressed in a grey square with a 100-unit side length, the obstacles are expressed by black objects and the yellow points stand for the unknown target landmarks. The perception range of each agent is set as 10 and the communication range is 2.5 times the perception range. Figure 1 presents two environment settings with different numbers of obstacles N_{ob} and two conditions of agents' start position. the number of agents N_a and the number of targets N_t are both fixed as 3.

(a) 1st configuration in Map 1   (b) 5th configuration in Map 2

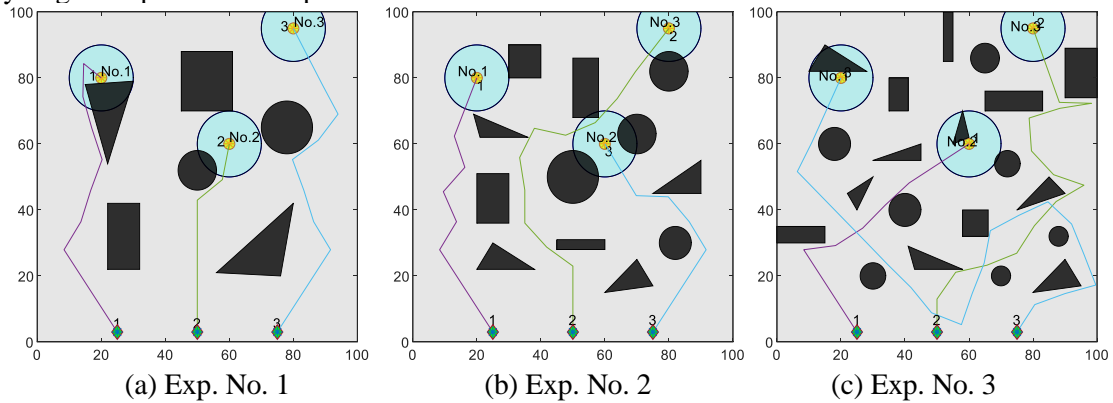**Figure 1.** Settings of environments, agents, and targets
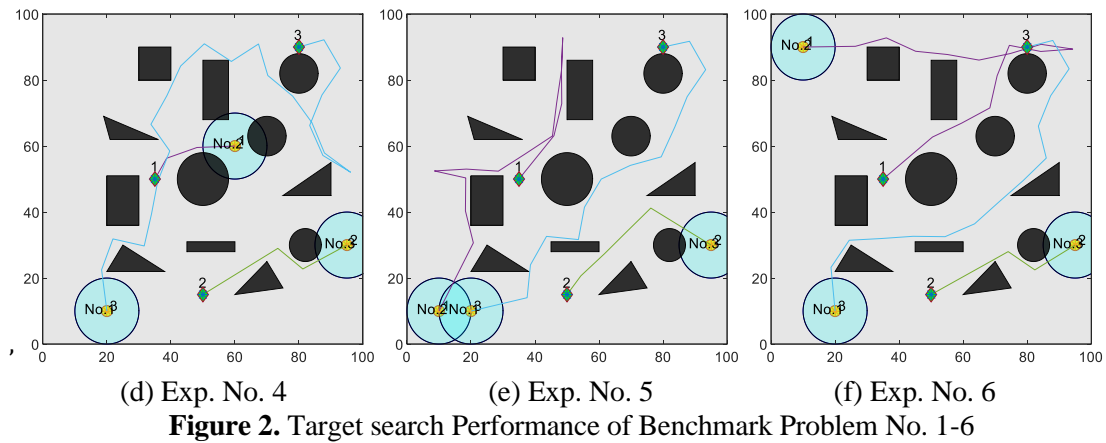
3.2. Experiment results

Considering different conditions of the number of obstacles in the environment and the initial distribution of agents and targets, six groups of experiments are designed and conducted. For verifying the reliability of experiment results, each group of experiments is repeated ten times. Table 1 presents the performance of the proposed strategy in terms of several performance indices: the task success rate which represents the reliability of the algorithm, agents' total travelled path lengths which indicate the energy consumption level in the exploration, and the total explored space area of the environment in the end. It can be observed that our virtual force-based strategy directs agents to reach the targets' vicinity location in a variety of configurations.

Table 1. Experimental results.

Exp. No.	N_{ob}	Targets Distribution	N_t	N_a	Initial positions	Average Path	Explored Space	Success Rate
1	6	Normal	3	3	Border	267.4	4983.7	100%
2	12	Normal	3	3	Border	294.0	5134.1	100%
3	20	Normal	3	3	Border	350.6	4924.2	100%
4	12	Normal	3	3	Inside	287.4	4329.1	100%
5	12	Sparse	3	3	Inside	537.1	5905.3	100%
6	12	Dense	3	3	Inside	489.1	5967.7	100%

Figure 2(a-c) shows that agents' average total travel length increases visibly with the number of obstacles increasing in the maps with even obstacle distributions. When all targets are successfully tracked, agents' cumulative explored area varies with the different map settings but keep at around 5000. Figure 2(d-f) illustrates the agents' exploration process in the map with normally distributed targets, sparsely distributed targets, and densely distributed targets individually. Table 1 presents the average travel path length of Exp. 5 and Exp. 6 is relatively large compared with Exp. 4.

(a) Exp. No. 1   (b) Exp. No. 2   (c) Exp. No. 3

(d) Exp. No. 4   (e) Exp. No. 5   (f) Exp. No. 6

Figure 2. Target search Performance of Benchmark Problem No. 1-6

5. Conclusion and future work

This paper addresses the task of searching targets in unknown environments using a small team of autonomous mobile robotics agents. A virtual force-based coordination strategy has been developed and investigated in the simulation environment as the defined problem configurations. This simple strategy relied on the local virtual force rules has demonstrated its effectiveness and efficiency successfully. The future work will involve extending it into a more complex map considering various targets' requirements and conducting experimental tests using mobile robots to further verify the effectiveness of the proposed approach.

6. References

[1] Y. Zou and K. Chakrabarty, "Sensor deployment and target localization based on virtual forces," in INFOCOM 2003. Twenty-Second Annual Joint Conference of the IEEE Computer and Communications. IEEE Societies, 2003, vol. 2, pp. 1293-1303: IEEE.

[2] X. Yu, W. Huang, J. Lan, and X. Qian, "A novel virtual force approach for node deployment in wireless sensor network," in Distributed Computing in Sensor Systems (DCOSS), 2012 IEEE 8th International Conference on, 2012, pp. 359-363: IEEE.

[3] X. Wang, S. Wang, and D. Bi, "Virtual force-directed particle swarm optimization for dynamic deployment in wireless sensor networks," in International Conference on Intelligent Computing, 2007, pp. 292-303: Springer.

[4] G. Sallam, U. Baroudi, and M. Al-Shaboti, "Multi-Robot Deployment Using a Virtual Force Approach: Challenges and Guidelines," Electronics, vol. 5, no. 3, p. 34, 2016.

[5] K. Ji, Q. Zhang, H. Cheng and D. Yu, "A Virtual Force Interaction Scheme for Monitoring Complex Unknown Environments by Autonomous Mobile Robots," *2019 18th European Control Conference (ECC)*, 2019, pp. 95-100, doi: 10.23919/ECC.2019.8795888.

Tammam Kaid

Postgraduate Researcher

School of Engineering

Integrated Modelling of Complex Material Systems

T Kaid, C Tang, J Guo, L Li, E. Elmshawet, J Ren

School of Engineering, Faculty of Engineering and Technology, Liverpool John Moores University
E-mail address: T.Kaid@2016.ljmu.ac.uk; C.Tang@2015.ljmu.ac.uk; J.Guo@ljmu.ac.uk; B.Li@ljmu.ac.uk; X.J.Ren@ljmu.ac.uk

Abstract. Microstructure based modelling at different length scales is important for data-driven materials development, quality control and process optimisation and a-driven research. This work reports an integrated approach for analysing structures of complex materials. The key function feature is presented covering source of microstructure data, image processing methods and different models of different scales. Some typical results are presented based welded hardfacing with multicomponent carbides. The key issues in analysing different material systems and functional properties are discussed with reference to future works.

Keywords: Microstructure, Finite Element Analysis, Multicomponent Carbides;

1. Introduction

The microstructure plays a crucial role in controlling the properties of material, including mechanical, physical and chemical properties. This is particularly relevant to materials with complex structures with secondary phases distributed within a matrix of distinctively different mechanical or physical properties. Example of which can be found in composites and alloys with complex carbide systems. Microstructural modelling has been applied to many different materials systems such as particulate composites, short fibre composite, electro spun polyurethane (PU) (Gorgi et al 2014; Wang et al 2016; Park et al, 2017). Park et al (2017) reported work on particulate composites using statistical synthetic structure and its thermo-mechanical finite element analysis. Wang et al (2016) utilised microstructure modelling to investigate the progressive failure behaviour of the material on the micro-scales. In the work, a new algorithm for generating random representative volume elements (RVEs) with statistical equivalent fibre distribution is used to generate the microstructures. With the development of computation models, complex data can be produced to support material design and development. The majority of works were focused on predicting generalised properties through homogenisation. Another important area is the study of the local phenomena. For example, Trias et al. (2006) demonstrated that random models must be considered for the simulation of local phenomena, as the use of periodic models leads to underestimation of matrix cracking and damage initiation. It is essential to develop approaches integrating both statistically representative structures as well the behaviour of individual particles within the matrix. This will not only provide more detailed data at small scales but offers new approach to extract more meaningful data for microstructure analysis and develop more meaningful data from the microstructures.

Most of the work has been based on composite structures in which the secondary phases are of a regular shape and defects free. But in some case, irregular shaped particles are use. One typical example is metal matrix composite, the ceramic particles used are often of different shapes (Villacorta-Hernández). Another important case is Cr-Fe-C system alloy, which consists of large primary carbides within a more ductile matrix formed during the sonification process during welding (Liu et al 2017). The properties of these systems are dependent on intrinsic properties of matrix and the reinforcement phases as well as pattern of distribution of the larger particles and the internal defects. An integrated modelling need to consider the overall structure and individual particles, thus improve the technical capacity in tuning the structure and properties through computational modelling. This paper reports the overall key functional blocks and methodology in developing microstructure-based FE models of those complex structures; Typical result based welded hardfacings with larger M7C3 carbides is presented and discussed. The key issues in analysing different material systems and properties is discussed with reference to future works.

2. Methodology

Microstructure concerned in this work is focused on the structure of a prepared surface of material. It can be representation of the material at different scales (mm-μm-nano), which provide information and data to simulate the behaviour of the material under different conditions. Figure 1 shows

Microstructure Data: Stereo microscope (SM) image, Optical Microscopy (OM); Scanning electron microscopy (SEM); Transmission electron microscopy (TEM); X-ray microtomography (XRM); Composition Mapping (e.g. Electron backscatter diffraction (EBSD)); Energy Despersive Spectroscopy (EDS) for elemental mapping.

the key functional block of program for microstructure-based FE modelling and analysis. The input could be based on different format; each could be taken at different length scales related to different material feature. Stereo microscope is suitable for structures at mm-μm scale (e.g. welded zones); Optical microscope could provide data on microstructures, scanning Electron microscope (mm-μm) could provide details of microstructure or interfaces between phases, transmission microscope is typically used for observation at nano scales or atomic length level. X-RM image could show material at micro and nano scales, while EBSD could provide data about the crystal orientation of the grains. EDS mapping shows the homogeneous distributions of elements that also reflect the material structure in 2D. All these could provide import structure data used to build structure models of the materials. The image processing section covered different approaches including Binary Image processing; Flood filled Processing; Canny edge detection; (hue, saturation, value/brightness) HSV. The use of different/hybrid approach will improve the robustness of the image processing. A curve fitting algorithm is applied to smoothing the interface between different phases through curve fitting, otherwise the step-wise pixel based feature would cause difficulties in the meshing process. In the model develop stage, the images could be used in two ways. The full field image can be used to produce the model, then the effective properties can be produced. Another approach is to study the individual particles. In some case, the model can also be made focusing on the interface. The interface properties can be produced integrating small scale modelling (for example first principle calculation to determine the ground state properties). Within the Abaqus, models can be produce to analyse mechanical. Thermal or electrical processes (ref???). The full field modelling approach is useful for material design and optimisation, while the modelling of individual particles is more useful for failure analysis, quality control.

Automatic Image Processing Programs: Binary Image processing; Flood filled Processing; Canny edge detection; HSV (hue, saturation, value/brightness)

FE modelling: Full field Model; Individual Particles Model; Full boundary/loading conditions; Representative Volume Element (RVE)conditions. Mechanical, Thermal, Electrical models.

Results and Data: Image data-particle distribution, Particle sizes; Mechanical-Density, Stiffness, Strength, Toughness, Stress distribution and concentration, Safety factor Thermal-Thermal conductivity, heat dissipation path/contours, thermal expansion, Electrical modelling: Electrical conductivity, current path, Resistance…

Practical use of the data: Structure design for properties; Quality control; Process optimisation.

Figure 1
Overall data system for developing microstructure-based FE models for linking structures to properties and performances.

3. Application of the microstructure modelling on welded hardfacings

| (a) Microstructure of Fe-Cr-C | (b)Binary Image processing | (c) Flood filled Processing |

Figure 2 *Typical microstructure of welded Fe-Cr-C alloys. (a) overall structure showing carbides of different shapes and structures. (b) a typical carbide showing the internal structures formed in a welding process.*

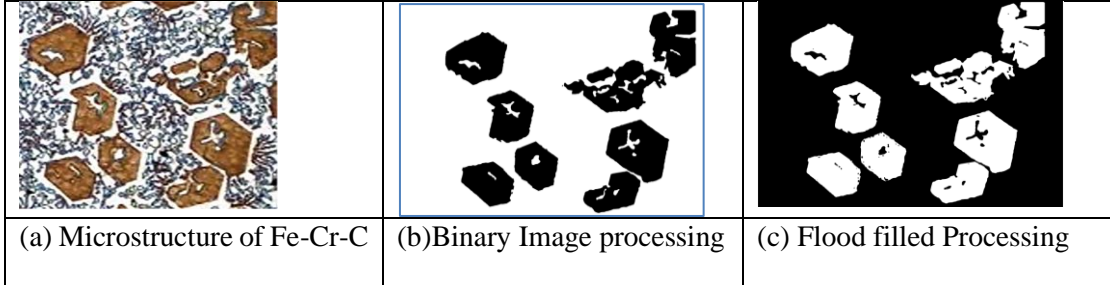A welded hardfacing is a functional layer applied to the surface of steel components to improve the wear or corrosion resistance. As shown in Figure 2(a), the structure of the hypereutectic Fe–Cr–C hardfacing alloy consists of a large quantity of large primary carbides 'M7C3' (where M could be Fe, Cr, i.e. (Fe, Cr)7C3) or other solution elements replacing Cr or Fe) within an eutectic matrix (Austenite+finer carbides). Typical images processed through Binary Image processing and flood filled processing is shown in Figure 2 (b) and (c), respectively. As shown in the figure the carbide has a base shape hexagonal as the M7C3 crystals follow a hexagonal lattice structure, however during the welding process, larger carbide may form through an aggregation process resulting in complex morphology (Liu et al 2016). One distinctive feature of the carbides in welded hardfacing lies in fact that these carbides has internal incomplete zones with an irregular contour and varying sizes, this made the image processing for FE modelling more complicated as the process need to accurate represent the interface. These internal feature may significantly affect the properties of the materials due to factors such as stress concentration, which can be assessed through predictive computation modelling.

Figure 3 shows typical model for the full field simulation approach. The modelling was conducted in Finite element package ABAQUS. The mesh was refined around the rim of the internal region/incomplete regions. A periodical boundary condition is applied treating the model as a representative volume (RVE), this effectively simulate the behaviour of the model mimicking the situation in a much larger specimen. Then, the effective properties of the material can be determined (isotropic, orthotropic or anisotropic properties) through a homogenisation process. As shown in the Figure (c), the whole field model is able to simulate the stress concentrations, and there are clear differences in the deformation and stresses of each individual carbides due to their difference in shape, size and internal features, which need to be quantified through more detailed local modelling.
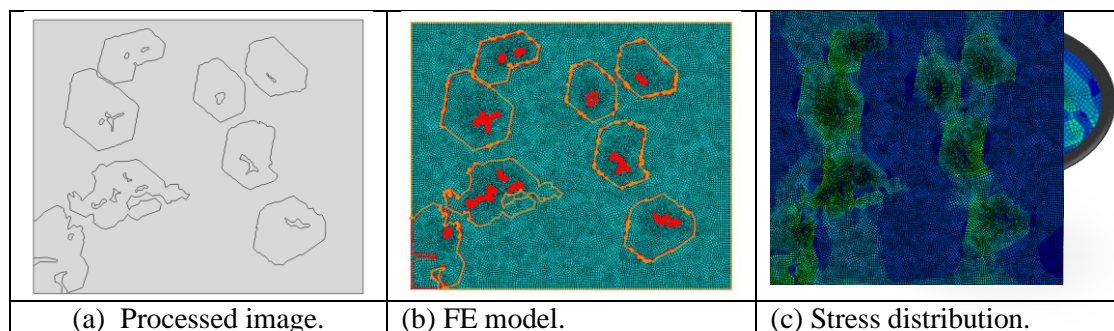

| (a) Processed image. | (b) FE model. | (c) Stress distribution. |

Figure 3 *Typical full field FE models and typical results.*

Figure 4 shows typical model and results individual carbide modelling approach. Given the carbides may subject to a complex loading condition in service along different orientations, different loading conditions can be applied to study more complex material behaviour such as stress concentration factors, yielding, fracture, etc. The program is developed to automatically identify the particles and develop the FE model for each individual carbides of interest. Models of two typical examples is shown in Figure 4 (a&b). Figure 4(a) illustrate a case of carbide with a regular Hexagonal shape but multiple internal features (incomplete region). Figure 4(b) shows a case of a carbide with irregular outline features but relatively simple internal feature. As shown by the contour of the stress distributions, the stress levels and the stress concentration factor of the secondary carbide (b) is clear higher than the case in (a). This highlighted that individual particle-based approach is essential when dealing with particle with complex internal features. The approaches have been applied to all the carbides and developed into a database reflecting the sensitivity of the carbide to fracture. Some typical data is illustrated in Figure 4(c), the stress concentration factor is calculated based on the average stress and the maximum stress in the carbides. It clearly shows that the stress concentration factor is significantly different between the carbides. This may directly affect the quality of the material. As the formation of carbides are associated with the composition and the processing parameters, the modelling data could offer information for materials design and process optimisation.
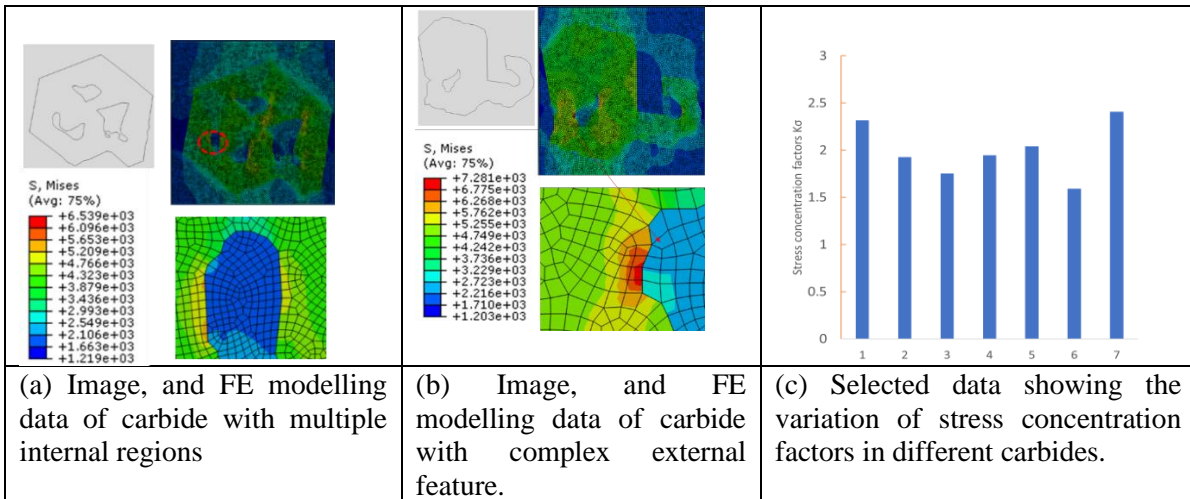
(a) Image, and FE modelling data of carbide with multiple internal regions	(b) Image, and FE modelling data of carbide with complex external feature.	(c) Selected data showing the variation of stress concentration factors in different carbides.

Figure 4 *Individual carbide model and typical results.*

4. Concluding remarks

In this work, an integrated microstructure-based FE approach is applied to analyse structures of complex M7C3 carbides in welded hardfacings. The source of microstructure data and image processing methods is presented and utilised in developing full-field and individual carbides models. The combined approach is effective to develop image and behaviour data of the carbides, which is important for materials design and process optimisation. The structure model and program can be used to study the thermal and electrical properties of the materials and other systems. Another area of work is to combine engineering modelling with physical modelling (atomic levels) to establish the effect of defects at the interface on the properties. The integration between modelling at different scales will contribute to data-led materials discovery and property by composition design.

References

Park H, Jung J and Kim H, 2017; *Comput. Mater. Sci.,* 126, 265-271

Wang W, Dai Y, Zhang C, Gao X, Zhao M, 2016, *Materials* 2016, 9(8), 624;

Trias, D.; Costa, J.; Mayugo, J.; Hurtado, J. 2006, *Comput. Mater. Sci.* 2006, 38, 316–324.

Villacorta-Hernández L, 2020, Technical Papers and Presentations, Comsol.com.

Liu S, Zhou Y, Xing X, Wang J, Ren X, Yang Q. 2016. *Scientific Reports*, 6.

Guo J, Feng Y, Liu L, Xing X, Ren X, Yang Q. 2016. *Wear*, 358-359 :137-147.

Neil Pickavance

Postgraduate Researcher

School of Civil Engineering and Built Environment

Critical Reflections on 25 Years of Using Prefabrication and Modularisation in UK Construction

Neil Pickavance

School of Civil Engineering and Built Environment, Faculty of Engineering & Technology, Liverpool John Moores University, Byrom Street, Liverpool, L3 3AF

n.m.pickavance@2017.ljmu.ac.uk

Abstract. Based on empirical evidence, this study draws on personal experience in an industry grappling with modern methods of construction between 1995 and the present day. A considerable lack of expertise is apparent within Government, associated bodies, and professional institutes, when it comes to applying knowledge and learning to the productivity problem, and offsite construction in particular. With a clear aim to provide a reflective account of P&M efficacy to explore value in programme delivery, the paper draws authentic experience into a research environment to allow an informed contribution to the topical conversation around offsite manufacturing, prefabrication, and modularisation, and debates its reputation as a panacea for construction's productivity challenge. The study critically reviews 35 examples of offsite construction, including precast frames, structural timber frames, prefabricated steel roof trusses, pre-assembled brickwork panels, prefabricated mechanical and electrical service modules (corridors and risers), hotel bathroom pods, fully modular offices, unitised glazed facades, package pumping stations, and attenuation tanks. Offsite manufacturing, prefabrication, and modularisation are used with some degree of success in the construction industry, however inefficiencies are common due to haphazard allocation plus a tendency to utilise on sections of work that possess programme float.

Keywords. Offsite, prefabrication, modularisation, programme, reflective

1. Introduction

This paper demonstrates that the use of prefabrication and modularisation in UK construction is flawed due to being consistently incorrectly allocated to elements of the project that possess programme float. Prefabrication and modularisation (P&M) in construction can be a method for shortening of the build programme. However, its selection, specification, and application can be haphazard and poorly thought out by contractors, consultants, clients, and developers. Decisions on P&M are influenced by various parties to the contract. These can be main contractors seeking productivity betterment, subcontractors selling their own product, or consultants seeking efficiency in the design. Factory quality, reduced site labour, and safer working are seen as further side-benefits. This investigation reflects on 25 years of empirical evidence.

2. Government and Industry Reports

2.1 Guidance, Policy, and Target Setting

Construction 2025 (HM Government 2013) [1] and Modernise or Die (Farmer 2016) [2] establish their own targets with no recommendations to support the challenge. The Industrial Strategy reports: Building a Britain fit for the future (HM Government 2017) [3] and Construction Sector Deal (HM Government 2018) [4] follow the format of promotion of offsite construction but offering no empirical supporting evidence. In these reports, offsite is placed in a wider context with other proposed modern methods of working and technologies to address productivity issues.

3. Literature Review

3.1 Offsite Manufacturing and Construction

Construction in the UK is characterised by low quality, high costs, a poor safety, adversarial nature, low investment in research and development, poor training, serviced by companies operating nationally and locally with low capital investment (Egan, 1998) [5]. In general, offsite construction is a modern method incorporating both prefabrication and preassembly or prefabrication of modules (Gibb 1999) [6] usually in a factory remote

from the project while groundworks, substructures, foundations, and suchlike are prepared on site. Offsite construction is increasingly gaining momentum in the UK construction industry, driven by the need for expedient delivery, technologically advanced approaches as well as government backing and influence (Siebert et al 2018) [7]. However, in the UK it is thought that no more than 2% of construction work has any significant adoption of prefabrication (Steinhardt and Manley 2016) [8].

Another significant benefit of adopting prefabrication is the reduction of onsite construction time due to the opportunity to simultaneously construct elements in the factory while the site-based work is progressing (Smith 2010) [9]. Goodier and Gibb (2007) [10] noted that longer lead times awaiting P&M elements could potentially delay the beginning of a project; to reduce this, the whole design and construction process needs to be better aligned. Goodier et al (2019) [11], in the proceedings of The Institute of Civil Engineers (Volume 172), provides awareness of the need to employ a decision-support tool when determining a project's suitability for offsite construction. The study notes that offsite and modular are increasing in engineering construction, and current decision-support tools are currently limited or outdated. To address this lack of process in construction, this paper presents a stage process for optimisation of prefabrication and modularisation for ensuring P&M is used on the project critical path.

4. Method

The 35 P&M elements are tabulated chronologically, with the sector type noted and the main year of installation (Table 1). Central to the study has been identifying whether or not the P&M element was on the project critical path, or not on the critical path, and thereby possessing float. These two conditions are identified in the table with Yes / No markings and any shortening to the overall construction programme is noted. Where shortening occurred, a percentage is provided in the table right-hand column to indicate the overall project saving compared to an equivalent traditional solution.

Table 1. Summary of research sample of 35 elements of P&M components.

P&M Element	Project Type	Year	Critical Path	Programme Shortening	Programme Saving
Package Pumping Stations	Industrial	1995	No	No	0%
Precast Concrete Retaining Wall	Retail	1997	No	No	0%
Precast Concrete Frame	Education	2000	YES	YES	23%
Precast Concrete Frame	Education	2000	YES	YES	23%
Precast Concrete Frame	Education	2000	YES	YES	23%
Precast Concrete Frame	Education	2000	YES	YES	23%
Precast Concrete Frame	Education	2000	YES	YES	23%
Precast Concrete Frame	Education	2000	YES	YES	23%
Precast Concrete Retaining Wall	Industrial	2000	No	No	0%
Modular Offices[1]	Industrial	2000	YES	YES	57%
Precast Concrete Piles	Education	2001	YES	YES	5%
Precast Concrete Frame	Education	2002	YES	YES	23%
Precast Concrete Frame	Education	2002	YES	YES	23%
Precast Concrete Frame	Education	2002	YES	YES	23%
Precast Concrete Frame	Education	2007	YES	YES	23%
M&E Modules (Corridors)	Education	2007	No	No	0%
Precast Concrete Lift Shafts	Leisure	2010	No	No	0%
Steel Roof Truss	Leisure	2010	No	No	0%
Steel Sheet Piles	Housing	2012	No	No	0%
Structural Insulated Panel System	Hotel	2012	No	No	0%
Bathroom Pods	Hotel	2012	Yes	No	0%
Precast Concrete Retaining Wall	Sports	2013	No	No	0%
Precast Concrete Terrace Units	Sports	2013	No	No	0%
Steel Footbridge	Sports	2014	No	No	0%
Plastic Service Chambers	Sports	2014	No	No	0%

Facing Brickwork Cladding Panels	Sports	2014	No	No	0%
Precast Concrete Stairs	Offices	2016	No	No	0%
Steel Cantilever	Offices	2016	No	No	0%
Unitised Glazing	Offices	2017	No	No	0%
Steel Staircase	Offices	2017	No	No	0%
Rooftop Cradle Access System	Offices	2017	No	No	0%
M&E Modules (Risers)	Offices	2017	No	No	0%
Structural Timber Frame	Restaurant	2017	YES	YES	5%
Attenuation Tank	Offices	2018	No	No	0%
Precast Concrete Stairs	Offices	2019	No	No	0%

[1] The Modular Offices, while shown in this table, are not a typical P&M component and are therefore not considered in the results, discussion, and conclusion sections.

5. Results / Discussion

The 35 individual elements reviewed, comprising 23 variants of P&M, yielded three P&M solutions with overall programme shortening (Table 2). This related to a P&M element being on the project critical path. Precast piles provided a saving of 2.5 weeks over bored piles, equating to 5% of the overall programme. The precast frame provided a saving of 5 weeks over a load-bearing brick and block frame, equating to 23% of the overall programme. The structural timber frame provided a saving of 2 weeks over steel, decking, and slabs, equating to 5% of the overall programme.

Table 2. Comparison of programme saving with P&M versus traditional.

Element	Duration	Saving	Project Saving
TRAD: CFA Bored Piles	3.5w	-	-
P&M: Precast Concrete Piles	1w	2.5w	2.5w off 55w (5%)
TRAD: Brick, Block, Plaster	6w	-	-
P&M: Precast Concrete Frame	1 w	5 w	5w off 22w (23%)
TRAD: Steel, Decking, Slabs	17w	-	-
P&M: Structural Timber Frame	15w	2w	2w off 38w (5%)

Figure 1(a) shows precast concrete piles at Ravensbury Primary School in east Manchester in 2001. Figure 1(b) is of precast concrete frame panels being erected to Beaver Road Primary School in south Manchester in 2000. Figure 1(c) is the structural timber frame being erected to The Pavilion at Spinningfields in Manchester in 2017.

Figure 1 (a) precast concrete piles; (b) precast concrete frame; (c) structural timber frame.

6. Conclusion

The current routes to specification, selection, and allocation of prefabrication and modularisation in UK construction supports programme underperformance. To obtain greater value through overall programme

shortening it was observed that this is almost exclusively achieved by utilising P&M elements on the project critical path. These programme gains were observed by specifying P&M solutions to precast piling, precast concrete frame, and structural timber frame. Allocating P&M elements to activities that have project float may serve to quicken localised sections of the programme but not shorten the overall programme duration. A combination of target-setting by Government and industry bodies, poor collaboration between contractors and consultants, and a lack of accurate, as-built feedback from projects allows an ignorance to flourish around P&M in the construction industry.

Government, chartered built environment institutes (CIOB, RICS, RIBA, ICE, CIBSE), and industry groups such as Constructing Excellence and UK Research and Innovation Council very much driven and dominated by self-published reports and recommendations that establish P&M aspirations for industry. There appears continuous target-setting with little contribution or awareness of the P&M selection process. A lack of expertise, knowledge, and learning around offsite construction by these bodies in general then provides some poor compensation with their attempts at referencing outdated P&M case studies.

Awareness of the need to employ a decision-support tool when determining a project's suitability for offsite construction is essential. With offsite and modular increasing in engineering construction, and current decision-support tools currently limited or outdated, addressing this lack of process in construction is crucial to drive value improvements.

7. References

[1] HM Government. "Industrial strategy: government and industry in partnership." *Construction 2025* (2013).

[2] Farmer, Mark. "Modernise or die." *London, Construction Leadership Council* (2016).

[3] HM Government. "Industrial strategy: Building a Britain fit for the future." *Government White Paper* (2017).

[4] HM Government. "Industrial strategy: Construction sector deal." *HM Government: UK* (2018).

[5] Egan, J. "Rethinking Construction. Department of the Environment." *Transport and the Regions* (1998).

[6] Gibb, Alistair GF. *Off-site fabrication: prefabrication, pre-assembly and modularisation*. John Wiley & Sons, 1999.

[7] Siebert, Michael, Lucelia Rodrigues, Mark Gillott, Emma Hines, and David Rich. "Identifying the barriers to change in the UK housebuilding industry." *Future Cities and Environment* 4, no. 1 (2018).

[8] Steinhardt, Dale A., and Karen Manley. "Adoption of prefabricated housing–the role of country context." *Sustainable cities and society* 22 (2016): 126-135.

[9] Smith, Ryan E. *Prefab architecture: A guide to modular design and construction*. John Wiley & Sons, 2010.

[10] Goodier, Chris, and Alistair Gibb. "Future opportunities for offsite in the UK." *Construction Management and Economics* 25, no. 6 (2007): 585-595.

[11] Goodier, Chris, Alistair Gibb, Mauro Mancini, Christoph Turck, Osman Gjepali, and Edwin Daniels. "Modularisation and offsite in engineering construction: an early decision-support tool." In *Proceedings of the Institution of Civil Engineers-Civil Engineering*, vol. 172, no. 6, pp. 3-14. Thomas Telford Ltd, 2019.